Exoplanets in the Antarctic Sky. I. The First Data Release of AST3-II (CHESPA) and New Found Variables within the Southern CVZ of *TESS*

Hui Zhang (□□)[1], Zhouyi Yu[1], Ensi Liang[1], Ming Yang[1], Michael C. B. Ashley[2], Xiangqun Cui[3,4], Fujia Du[3,4], Jianning Fu[5], Xuefei Gong[3,4], Bozhong Gu[3,4], Yi Hu[4,6], Peng Jiang[7,8], Huigen Liu[1], Jon Lawrence[9], Qiang Liu[6], Xiaoyan Li[3,4], Zhengyang Li[3,4], Bin Ma[4,6,10], Jeremy Mould[11,12], Zhaohui Shang[4,6,13], Nicholas B. Suntzeff[14], Charling Tao[15,16], Qiguo Tian[17], C. G. Tinney[18], Syed A. Uddin[19], Lifan Wang[4,14,19], Songhu Wang[20], Xiaofeng Wang[16], Peng Wei[1], Duncan Wright[21], Xuefeng Wu[4,19], Robert A. Wittenmyer[21], Lingzhe Xu[3], Shi-hai Yang[3,4], Ce Yu[22], Xiangyan Yuan[3,4], Jessica Zheng[23], Hongyan Zhou[17], Ji-lin Zhou[1], and Zhenxi Zhu[4,19]

[1] School of Astronomy and Space Science, Key Laboratory of Modern Astronomy and Astrophysics in Ministry of Education, Nanjing University, Nanjing 210023, Jiangsu, People's Republic of China; huizhang@nju.edu.cn, zhoujl@nju.edu.cn [2] School of Physics, University of New South Wales, NSW 2052, Australia [3] Nanjing Institute of Astronomical Optics and Technology, Nanjing 210042, People's Republic of China [4] Chinese Center for Antarctic Astronomy, Nanjing 210008, People's Republic of China [5] Department of Astronomy, Beijing Normal University, Beijing, 100875, People's Republic of China [6] National Astronomical Observatories, Chinese Academy of Sciences, Beijing 100012, People's Republic of China [7] Polar Research Institute of China, Shanghai 200136, People's Republic of China [8] Chinese Center for Antarctic Astronomy, 451 Jinqiao Rd., Nanjing 210008, People's Republic of China [9] Australian Astronomical Optics, Macquarie University, NSW 2109, Australia [10] University of Chinese Academy of Sciences, Beijing 100049, People's Republic of China [11] Centre for Astrophysics and Supercomputing, Swinburne University of Technology, P.O. Box 218, Mail Number H29, Hawthorn, VIC 3122, Australia [12] ARC Centre of Excellence for All-sky Astrophysics (CAASTRO), Australia [13] Tianjin Astrophysics Center, Tianjin Normal University, Tianjin 300387, People's Republic of China [14] George P. and Cynthia Woods Mitchell Institute for Fundamental Physics & Astronomy, Texas A&M University, Department of Physics and Astronomy, 4242 TAMU, College Station, TX 77843, USA [15] Aix Marseille Univ., CNRS/IN2P3, CPPM, Marseille, France [16] Physics Department and Tsinghua Center for Astrophysics (THCA), Tsinghua University, Beijing, 100084, People's Republic of China [17] Polar Research Institute of China, 451 Jinqiao Rd., Shanghai 200136, People's Republic of China [18] Exoplanetary Science at UNSW, School of Physics, UNSW Sydney, NSW 2052, Australia [19] Purple Mountain Observatory, Nanjing 210008, People's Republic of China [20] Department of Astronomy, Yale University, New Haven, CT 06511, USA [21] University of Southern Queensland, Computational Engineering and Science Research Centre, Toowoomba, QLD 4350, Australia [22] School of Computer Science and Technology, Tianjin University, Tianjin 300072, People's Republic of China [23] Australian Astronomical Observatory, 105 Delhi Road, North Ryde, NSW 2113, Australia

Abstract

Located at Dome A, the highest point of the Antarctic plateau, the Chinese Kunlun station is considered to be one of the best ground-based photometric sites because of its extremely cold, dry, and stable atmosphere. A target can be monitored from there for over 40 days without diurnal interruption during a polar winter. This makes Kunlun station a perfect site to search for short-period transiting exoplanets. Since 2008, an observatory has existed at Kunlun station, and three telescopes are working there. Using these

telescopes, the AST3 project has been carried out over the last 6 yr with a search for transiting exoplanets as one of its key programs (CHESPA). In the austral winters of 2016 and 2017, a set of target fields in the southern continuous viewing zone (CVZ) of *TESS* were monitored by the AST3-II telescope. In this paper, we introduce the CHESPA and present the first data release containing photometry of 26,578 bright stars ($m_i \leqslant 15$). The best photometric precision at the optimum magnitude for the survey is around 2 mmag. To demonstrate the data quality, we also present a catalog of 221 variables with a brightness variation greater than 5 mmag from the 2016 data. Among these variables, 179 are newly identified periodic variables not listed in the AAVSO database (https://www.aavso.org/), and 67 are listed in the Candidate Target List. These variables will require careful attention to avoid false-positive signals when searching for transiting exoplanets. Dozens of new transiting exoplanet candidates will be released in a subsequent paper.

Key words: binaries: eclipsing – catalogs – planets and satellites: detection – stars: variables: general – surveys – techniques: photometric

1. Introduction

Wide-field photometric surveys for transit signals have proved to be one of the most effective methods for finding exoplanets. To date, more than 80% of known exoplanets have been discovered by photometric surveys using either ground- or space-based telescopes, with the *Kepler* project (Borucki et al. 2010) contributing the largest fraction of these transiting exoplanets. Besides just making new discoveries, photometric surveys provide key physical characteristics of exoplanets: the transit depth reveals the physical size of the transiting planet (relative to the host star), which is crucial in determining its nature (i.e., is it a gas giant or a super-Earth?), while the shape of the transit event indicates the orbit's impact parameter, constraining the orbital inclination of the planet and providing insight into the dynamical evolution of the planetary system (Seager & Mallén-Ornelas 2003). When coupled with dynamical masses determined from radial velocities of the host star, photometric measurements reveal the average density of the planet and hence constrain its composition and internal structure (see, e.g., Seager et al. 2007; Baraffe et al. 2008). Ultra-high-precision photometry can reveal secondary eclipses and phase curves. These provide a unique way to measure the reflected and thermal emission of an exoplanet, leading to estimates of its surface albedo and allowing modeling of the heat transport efficiency (see, e.g., Charbonneau et al. 2005; Deming et al. 2005; Knutson 2007). Combining all the information possible from photometry, we can establish a relatively detailed model of the exoplanet's atmosphere and hence its possible habitability.

To search for and study exoplanets using photometry, a survey needs a wide field of view (FOV), high photometric precision, and as complete time coverage of the obrial periods of interest as possible. Some pioneering

ground-based projects have been very successful, e.g., WASP/SuperWASP (Pollacco et al. 2006), HATNET (Bakos et al. 2004), HATSouth (Bakos et al. 2013), and KELT (Pepper et al. 2007). Hundreds of transiting exoplanets have been found from such efforts over the last two decades. These surveys have shown that stable instruments (e.g., low systematic errors, long time stability), optimized operations (e.g., well-organized duty cycle, precise autoguiding), and superb observing conditions (e.g., good seeing, fewer interruptions from bad weather) are crucial for producing high-quality light curves and thus reducing the number of false positives in lists of transiting exoplanet candidates.

On one hand, with experience gained and new technologies adopted, new-generation wide-field transit surveys have overcome many obstacles in both hardware and software, e.g., NGTS (Wheatley et al. 2018) and Pan-Planets (Obermeier et al. 2016). On the other hand, a good observing site is still essential to guarantee a fruitful survey, and this is where the Antarctic Plateau has many advantages over traditional temperate-latitude sites. The extremely cold atmosphere in Antarctica from the telescope up leads to very low and very stable water vapor content, which reduces photometric noise from varying water absorption. The decreased high-altitude turbulence above the plateau results in dramatically reduced scintillation noise (Kenyon & Storey 2006). This combination makes the Antarctic Plateau an ideal place to perform optical, infrared, and THz observations. Lawrence et al. (2004) reported a median seeing of $0\farcs23$ (average of $0\farcs27$) above a 30 m boundary layer at Dome C, drawing worldwide attention. Subsequently, many studies have been made of the astronomical conditions at various Antarctic sites; for a summary, see Storey et al. (2005), Burton et al. (2007), and Ashley (2013). Saunders et al. (2009) studied eight major factors, such as the boundary layer thickness, cloud coverage, auroral emission, airglow, atmospheric thermal backgrounds, precipitable water vapor, telescope thermal backgrounds, and the free-atmosphere seeing, at Domes A, B, C, and F and Ridges A and B. After a systematic comparison, they concluded that Dome A, the highest point of the Antarctic Plateau, was the best site overall. Besides the excellent photometric conditions, the polar night in Antarctica provides an opportunity to stare at a target field for over 40 days without interruption from the diurnal cycle. This is a great advantage to enhance the detectability of short-period transiting exoplanets.

Since the first visit to Dome A in 2005 by the 21st CHInese National Antarctic Research Expedition (CHINARE), Chinese astronomers and their international collaborators have performed a series of site-testing studies. The results from multiple experiments have shown that Dome A has a thin boundary layer with a 14 m median height (Bonner et al. 2010), a strong temperature inversion above the snow surface, low wind speed (Hu et al. 2014), low water vapor (Shi et al. 2016), low sky brightness, and a high clear-sky fraction (Zou et al. 2010; Yang et al. 2017). These results are consistent with previous predictions made largely from satellite observations by Saunders et al.

(2009). The first-generation telescope at Dome A (the Chinese Small Telescope ARray (CSTAR); Yuan et al. 2008; Zhou et al. 2010) was installed in 2008. The CSTAR produced more than 200,000 continuous images on a fixed FOV of 4.°5 × 4.°5 centered at the south celestial pole in the austral winters of 2008, 2009, and 2010. After a series of refinements (such as corrections for the inhomogeneous effects of clouds and the treatment of ghost images and diurnal effects; Wang et al. 2012, 2014b; Meng et al. 2013), a photometric precision of 4 mmag was obtained for bright stars in CSTAR data. Hundreds of new variable stars were identified and studied from these data (e.g., Wang et al. 2011; Yang et al. 2015; Zong et al. 2015; Liang et al. 2016; Oelkers et al. 2016), and the first six exoplanet candidates around the south celestial pole were identified (Wang et al. 2014a). Based on this successful experience and lessons learned from the CSTAR project, a second generation of telescopes—the Antarctic Survey Telescopes (AST3)—were conceived for a wide-field, high-resolution photometric survey at Dome A. The AST3 was envisaged as three 50 cm aperture telescopes, each with a different fixed filter. The AST3 telescopes not only have larger apertures than CSTAR, they also have full tracking systems and higher angular resolutions (~1'' pixel^{-1}), which provide wider sky coverage and better precision. The first and second AST3 telescopes—AST3-I and AST3-II—were installed at Dome A in 2012 and 2015 by the 28th and 31st CHINARE (respectively). Observing programs with AST3-I have been described by Liu et al. (2018) and the corresponding data published by Ma et al. (2018). The third AST3 telescope is nearing completion in Nanjing and will be equipped with a Kdark-band near-infrared camera (Burton et al. 2016). Using the CSTAR and AST3 telescopes, we have started a long-term wide-field photometric survey searching for transiting exoplanets in the Antarctic sky: the Chinese Exoplanet Searching Program from Antarctica (CHESPA).

In the austral winters of 2016 and 2017, we used the AST3-II telescope to survey a group of selected fields near the southern ecliptic pole and within the southern continuous viewing zone (CVZ) of *TESS* (Ricker et al. 2009). In this first paper, we describe the observations obtained and data reduction processes used on them, as well as presenting some of the data products obtained in 2016. This data release includes reduced images, calibrated catalogs, and detrended light curves of 26,578 bright ($7.5 \leq mi \leq 15.0$) stars near the southern ecliptic pole. We also present a catalog of variable stars found in the southern CVZ of *TESS*. Since wide-field surveys for transiting exoplanets often suffer from large pixel scales and are notoriously plagued by false positives, high-resolution photometric follow-up observations are necessary to filter out objects such as eclipsing binaries. The precision of *TESS* is expected to be much better than that of ground-based surveys; however, its pixel scale is still relatively large, ~21'' pixel^{-1}, and a high false-alarm rate caused by blending events such as background eclipsing binaries is expected (Collins et al. 2018). Our catalog of variables will be a good reference for identifying these blending events. In this work,

we only present obvious binaries and pulsating stars with regular periods. A detailed classification and analysis of other variables, e.g., rotational spots modulation, semiperiodic/irregular variables, and long-period variables, will be available soon in a series of subsequent papers. The description of the light curve detrending, transit signal search, and a detailed catalog of transiting exoplanet candidates will be presented by Zhang et al. (2018). Results for observations of specific targets, e.g., Proxima Centauri and β Pictoris, will also be released in the near future.

This paper is organized as follows. We introduce the instruments and our survey strategy in Section 2, we describe the survey strategy and observations in Section 3, the detailed data reduction flow is described in Section 4, we present the survey results in Section 5, and we summarize the paper in Section 6.

2. The Instruments

The AST3-I telescope was designed and built by the Nanjing Institute of Astronomical Optics and Technology (NIAOT); see Cui et al. (2008), Yuan et al. (2014, 2015), and Wang et al. (2017) and references therein for more details. The AST3-II telescope (which was used to acquire all the data used in this work) is the second of the three planned AST3 telescopes. It is almost identical to AST3-I: they share the same modified Schmidt system design (Yuan & Su 2012), entrance pupil aperture of 50 cm, wide FOV of 4.3 $\deg^2$, Sloan *i* filter, and CCD camera. Some improvements and innovations have been made in AST3-II in the area of focusing, snowproofing, and the defrosting system based on our experience from the earlier operations of AST3-I during austral winters since 2012. Thanks to these updates, AST3-II worked well during the extremely cold winters of 2016 and 2017 and has acquired over 30 TB of high-quality images. A single raw AST3-II image is 10K × 5K pixels in size, using 122 MB of storage. It is generated by a 10K × 10K frame transfer STA1600FT CCD camera with a pixel scale of ~1'' pixel^{-1} over an FOV of 1.5 × 2.9 $\deg^2$ (R.A. × decl.). The average FWHM of stars obtained by focused AST3 telescopes is around ~2.0 pixels. The CCD detector operates in frame transfer mode without a shutter and is divided into frame store regions (in its top and bottom quadrants) and an active imaging area in its central half. Although this configuration halved the maximum possible FOV, it eliminates the risk of shutter mechanism failure. Since the telescope has to be operated entirely remotely for 11 months with no possibility of repairs being carried out, any mechanism failure would be fatal to the whole project, and the shutter is one of the most fragile parts of these high-frequency observations. The image area of the CCD has 16 readout channels, each 1500 × 2650 pixels (including overscan regions). A full-frame raw image is shown in Figure 1, and more details on the AST3 CCD performance can be found in Ma et al. (2012) and Shang et al. (2012).

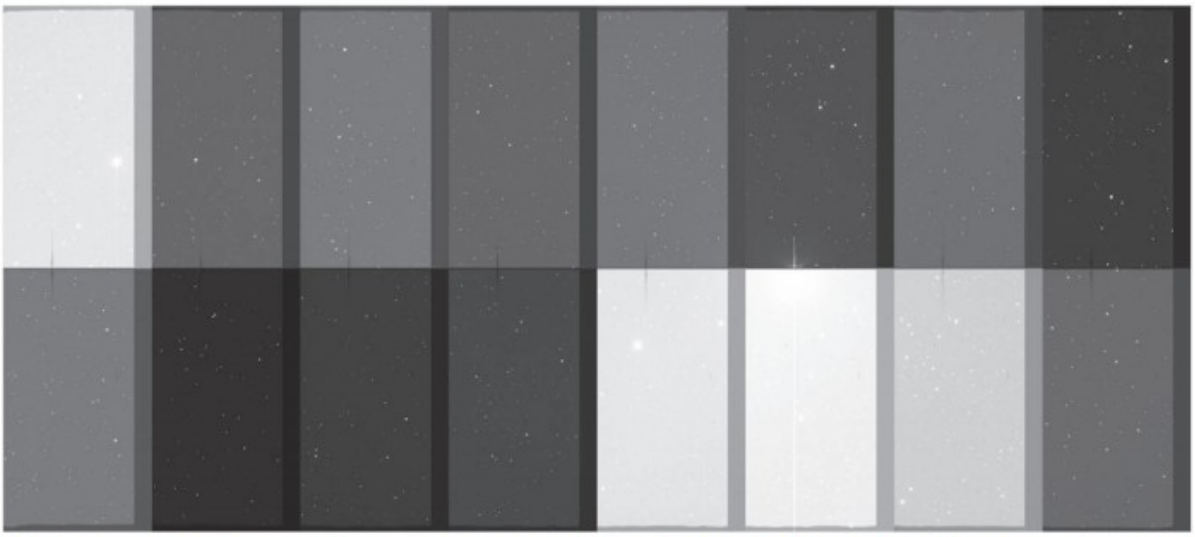

Figure 1. Full frame of a raw image taken by AST3-II. There are 16 readout channels: eight at the top and eight at the bottom. Each channel has a physical resolution of 1500 × 2650 pixels, including overscan regions. Dark gaps between channels are those overscan regions that are extra pixels generated by the CCD electronics when the CCD is read out. They are not connected to real physical pixels on the CCD but can be used to estimate the bias of the image. Each gap will be modeled and subtracted from the readout channel to the left (see Section 4.1.1 for details). All of these overscan regions are trimmed off during the data reduction processes.

During the austral winter observing season, the whole AST3 system is operated remotely, and the scheduled observations are executed in a fully automatic mode. Consequently, safety, reliability, and stability are key issues for the AST3 design. The core systems, consisting of the main control computer, storage disk array, and pipeline computer, were intensively customized to handle almost any conceivable hardware, software, or network failure. Each component in the system had two identical copies for redundancy, minimizing the risk to the system from single-point failures. As an example, the fiber optic data link from the CCD camera was split into two fibers so that two separate computers could be used to control the CCD. The hardware and software for the operation, control, and data (COD) system were developed by the National Astronomical Observatories, Chinese Academy of Sciences (NAOC; Shang et al. 2012; Hu et al. 2016). The electrical power supply and internet communication were provided by a similarly reliable on-site observatory platform, PLATO-A, which is an improved version of UNSW's automated PLATO observatory platform for CSTAR and other earlier instruments. PLATO-A was designed to provide a continuous 1 kW power source for the AST3 telescopes (Lawrence et al. 2009; Ashley et al. 2010) for at least 1 yr without servicing.

3. The Exoplanet Survey Program

The *Kepler* project has dramatically broadened our horizons in exoplanet science over the last 5 yr. Although it has surveyed only a small part of the sky, its unprecedented photometric precision and continuous observing capability have been superbly successful at discovering planets down to Earth sizes. However, most candidates found by *Kepler* are just too faint to be followed up with dynamical mass measurements from the

ground. *Kepler*'s successor mission, *TESS*, will be similarly revolutionary, albeit in a different way—by surveying the whole sky for short-period transiting exoplanets orbiting bright and/or nearby stars that can be followed up with dynamical masses from the ground. *TESS* launched on 2018 April 18 and started surveying all bright stars in the southern hemisphere in 2018 June. Thousands of exoplanet candidates are expected to be detected over the next 2 yr. However, to achieve whole-sky coverage, *TESS* must use a large pixel scale (~21'' pixel^{-1}), which may lead to a higher false-alarm rate than *Kepler*. Many candidates detected by *TESS* may be astrophysical mimics, e.g., blended eclipsing binaries. Therefore, high-resolution photometric follow-up observations are necessary before undertaking time-consuming and competitive radial velocity observations to measure dynamical masses. The AST3 telescopes were designed to perform wide-field (FOV ~ 4.3 deg^2) and high-resolution (pixel scale ~1'' pixel^{-1}) time-domain photometric surveys and are well suited to this task. The observational conditions and uninterrupted polar nights at Dome A deliver additional benefits for this science.

To maximize the scientific value of our program, we select 48 fields within *TESS*'s southern CVZ (which is centered at the southern ecliptic pole at R.A. = 06^{h}00^{m}00^s, decl. = −66°33'00''). These fields are scientifically important because (in addition to their southerly decl., meaning they can be observed from Dome A at low airmasses) they will be observed by *TESS* uninterrupted for 12 months. This long observing baseline will greatly increase *TESS*'s sensitivity for short-period exoplanets, as well as allowing the detection of long-period planets in single-star and binary systems (Stassun et al. 2018). Additionally, the CVZ of *JWST* will also be located in this region, so any targets of interest will be studied by much more intensive detailed follow-up in the future.

Our selected fields were numbered and divided into three groups, with each group being scheduled to be surveyed for a whole austral winter in 2016, 2017, and 2018, respectively (see Figure 2). Fields close to the Large Magellanic Cloud (LMC) were excluded because they are too crowded and most bright stars in the LMC will be giants, making transiting exoplanet signals exceedingly weak. From 2016 May 16 to June 22, we scanned the first group of 10 adjacent fields (AST3II004—AST3II013; see Table 1). The available dark time increased day by day during the first half of our observation campaign, and it finally became 24 hr a day at the end of June. A part of the very dark nights were spent on the other programs searching for transient targets, e.g., supernovae. After excluding interruptions caused by bad weather and regular instrument maintenance, we observed for more than 350 hr spanning 37 nights (Figure 3). The overall operation coverage is ~40%, which is less than the coverage we expected: ~75%. In 2017, we spent most of the nights where weather and instrumentation were suitable on CHESPA, and its working coverage reached ~80%. To avoid saturation by bright stars and to reduce the electromagnetic interference in our CCD

images (see Section 4.1.4), we adopted a short-exposure stacking strategy. In each observing night, we started from field AST3II004 and took three consecutive 10 s exposures, then moved to field AST3II005 and repeated, then moved to AST3II006, and so on. When the last field—AST3II013—completed, we jumped back to the first field—AST3II004—and started a new loop. The dead time between each field was about 72 s, including three 16 s readout intervals and a 24 s slewing operation. Every three adjacent images of the same field were median combined to achieve a high signal-to-noise ratio (S/N). Thus, the overall sampling cadence was about 12 minutes for each field.

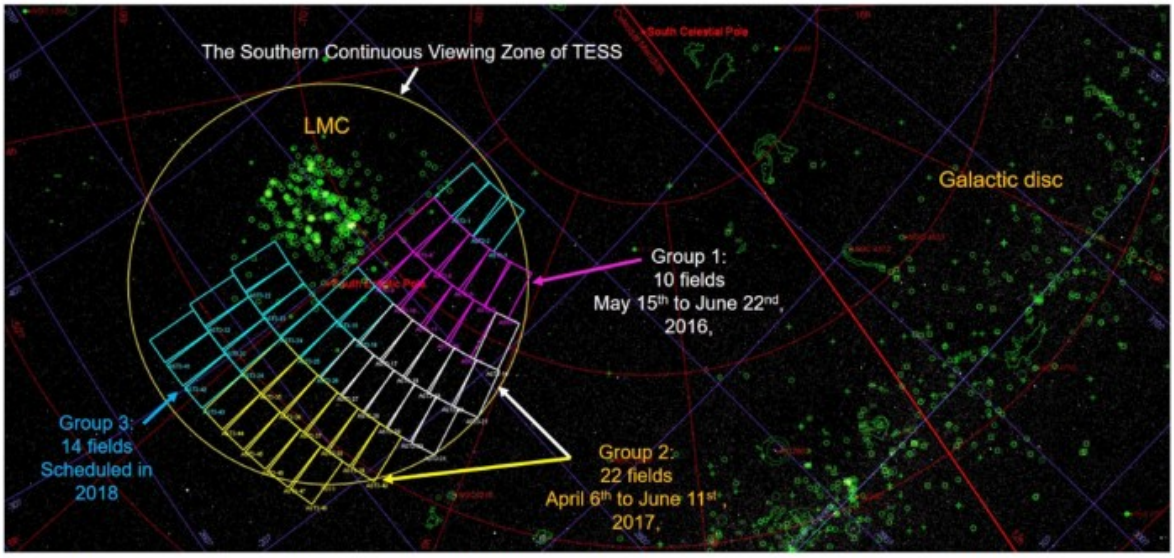

Figure 2. Planned survey of 48 target fields in 2016, 2017, and 2018. Each field has a sky coverage of ~4.3 deg^2. Fields close to the LMC are excluded to avoid crowded fields of giant stars. Group 1 (10 fields) and group 2 (22 fields) were scanned in 2016 and 2017, respectively.

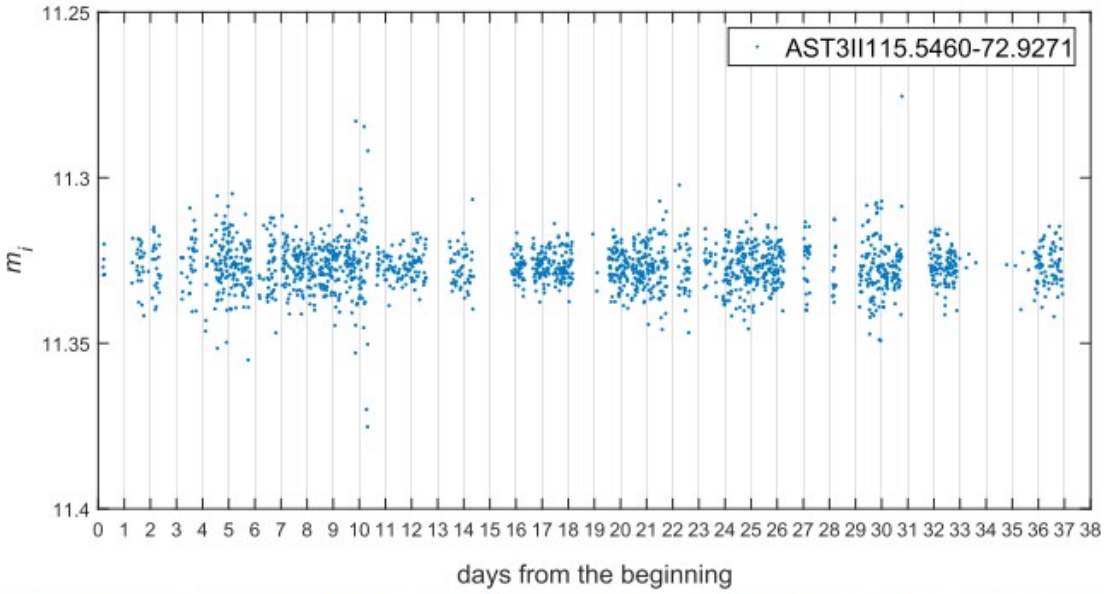

Figure 3. Light curve of target "AST3II115.5460-72.9271," which is a newfound eclipsing binary. The sampling cadence is 12 minutes. A detrended, binned, and phase-folded light curve of this target can be found in Figure 16. The x axis shows the days from the beginning of the survey. Thanks to the polar nights, our observation may span several days without interruption by daylight. The gaps between continuous observations are caused by bad weather, instrument maintenance, and other surveys.

Table 1
Center Coordinates of 10 AST3-II Target Fields Surveyed in 2016

Field Name	Field Center		Valid Images
	R.A. (J2000.0)	Decl. (J2000.0)	
AST3II004	93.000	−73.000	3179
AST3II005	98.500	−73.000	3080
AST3II006	104.000	−73.000	3049
AST3II007	109.500	−73.000	3103
AST3II008	115.000	−73.000	3248
AST3II009	93.000	−70.000	3090
AST3II010	97.750	−70.000	3000
AST3II011	102.500	−70.000	2991
AST3II012	107.250	−70.000	3021
AST3II013	112.000	−70.000	3128

Twilight-sky frames were taken at each dawn and dusk during the periods when the Sun was still rising each day at Dome A. These sky frames were combined to produce a master flat-field image (see Section 4.1.3). However, fluctuations in the super-sky flat field are a major source of systematic noise for wide-field surveys. To reduce this, we first adopted a moderate defocusing of the telescope. The average seeing on the ground of Dome A is estimated to be around ~1'' or better. Convolved with the optics of a telescope, the actual size of the point-spread functions (PSFs) of stars is usually larger than the seeing. So the AST3-II pixel scale of 1'' pixel^{-1} is designed to be better than the average FWHM of stars acquired by the focused AST3-II at Dome A, which is around ~2.0 pixels. During the exoplanet survey, we adjusted the focus to produce star images with PSFs

between FWHM = 3 pixels and FWHM = 5 pixels. The shapes and sizes of the star images vary with the environment temperature, airmass, and etc. Sometimes, the PSF deviates from the standard Gaussian profile and forms a flat top. But it does not cause much of a problem, since we adopt aperture photometry. For each star, the variations in the FWHM, elongation,[24] and fraction-of-light radius[25] are recorded. In the later external parameter detrending (EPD) process, these variations will be detrended from the light curve. Second, a semi-autoguiding method was adopted. For each field, a template image with a well-determined astrometric solution is constructed before the survey begins. Every time the telescope points to a new field, the first image of this field is cross-matched with its template, and offsets are fed back to the pointing model and the two following images acquired after this pointing correction. The interval between two pointing corrections is the same as the dead time between moving fields, i.e., every ~72 s. Within this short time, the position variation of a star is still less than the average size of a PSF, FWHM ~ 4 pixels. Even so, it is still very difficult to fix stars to the same pixels during the entire observation campaign. Finally, we detrend the brightness variation of each star against its inter- and intrapixel position changes and variances to further reduce any systematic error caused by position shifting of stars.

The telescopes working at Dome A are entirely unattended during the year, apart from about 3 weeks over summer when servicing is performed on-site. The internet connection to Dome A relies on the Iridium satellite system, which has a typical latency of about 2 s and can occasionally drop out and take up to 1 minute to reconnect. The operation of the telescope and CCD is therefore controlled automatically from scripts running on-site at Dome A. The whole system can be shifted to manual control from China if required (e.g., if the telescope optics and/or gear mechanisms need defrosting). Images taken by AST3-II are stored on a disk array on-site. The bandwidth of the Iridium connection makes it impractical to download even a single whole image, so we only perform relatively simple data reduction processes on-site —e.g., to check data quality and set up alarms for specific events. The detailed reduction of the entire data set waits until the hard drives are physically returned by the expedition team in April or May of the following year.

At the end of the exoplanet survey program in 2016, more than 35,000 science frames were taken by the AST3-II telescope. Some statistics on the data quality are shown in Figure 4. We removed images with flaws including high sky backgrounds, a large fraction of saturated area, large average FWHM (>6 pixels), large average elongations (>2), and small numbers of detectable stars (<500). After this quality filtering, 30,889 high-quality images remained. They were further reduced and coadded to produce 18,729 science images. Catalogs of these images were matched with a master catalog generated from the APASS database (Henden et

al. 2015, 2016). Finally, light curves for 26,578 stars brighter than Sloan $\boldsymbol{m}i$ = 15 mag were extracted.

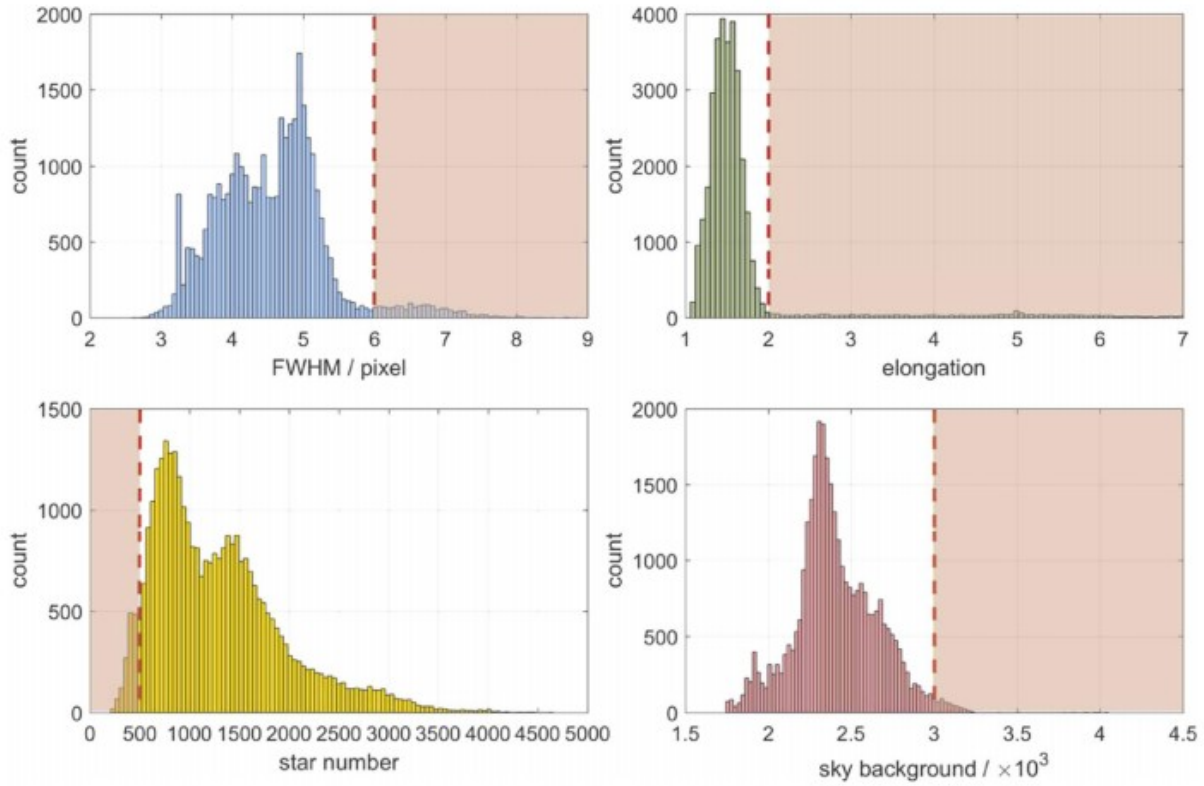

Figure 4. Statistics of image qualities. Images within the shadowed region were dropped to maintain high data quality.

4. Data Reduction Pipeline

The on-site power budget and limited computational resources mean we only run a simple on-site data reduction pipeline including only standard image processes, such as overscan subtraction, flat-field correction, and simple-aperture photometry using Sextractor (Bertin & Arnouts 1996). Reduced catalogs are then downloaded through the Iridium satellite connection while observing. However, the limited connection bandwidth and monthly quota mean only the catalogs of selected fields are downloaded. We perform further astrometric solutions and flux calibration on these catalogs and extract light curves of selected targets. Although the precision of this on-site data reduction is not optimal, it does return rms ~1% light curves, which are useful for inspecting the daily data quality and triggering alarms of highly valuable targets (e.g., potential transit events of β Pictoris and Proxima Centauri). As described above, full data processing awaits the return of the data on hard drives from Dome A.

A detailed data reduction flowchart for this full processing is shown in Figure 5. The pipeline consists of five major components, which are described below: (1) image reduction, which produces cleaned, WCS solved, and coadded science images; (2) catalog processing, which produces flux-

calibrated catalogs; (3) light-curve detrending, which produces light curves for general scientific usage; (4) periodic signal searching, which searches for periodic variables and generates the variables catalog that is published in this work; and (5) transit signal searching, which polishes the light curves further, searches for transit-like signals, and validates exoplanet candidates. The pipeline operates in the MATLAB environment and has been fully parallelized. Some functions from well-tested open-source packages are used, including Sextractor (Bertin & Arnouts 1996), Swarp (Bertin et al. 2002), VARTOOLS (Hartman & Bakos 2016), and Astrometry.net (Lang et al. 2010).

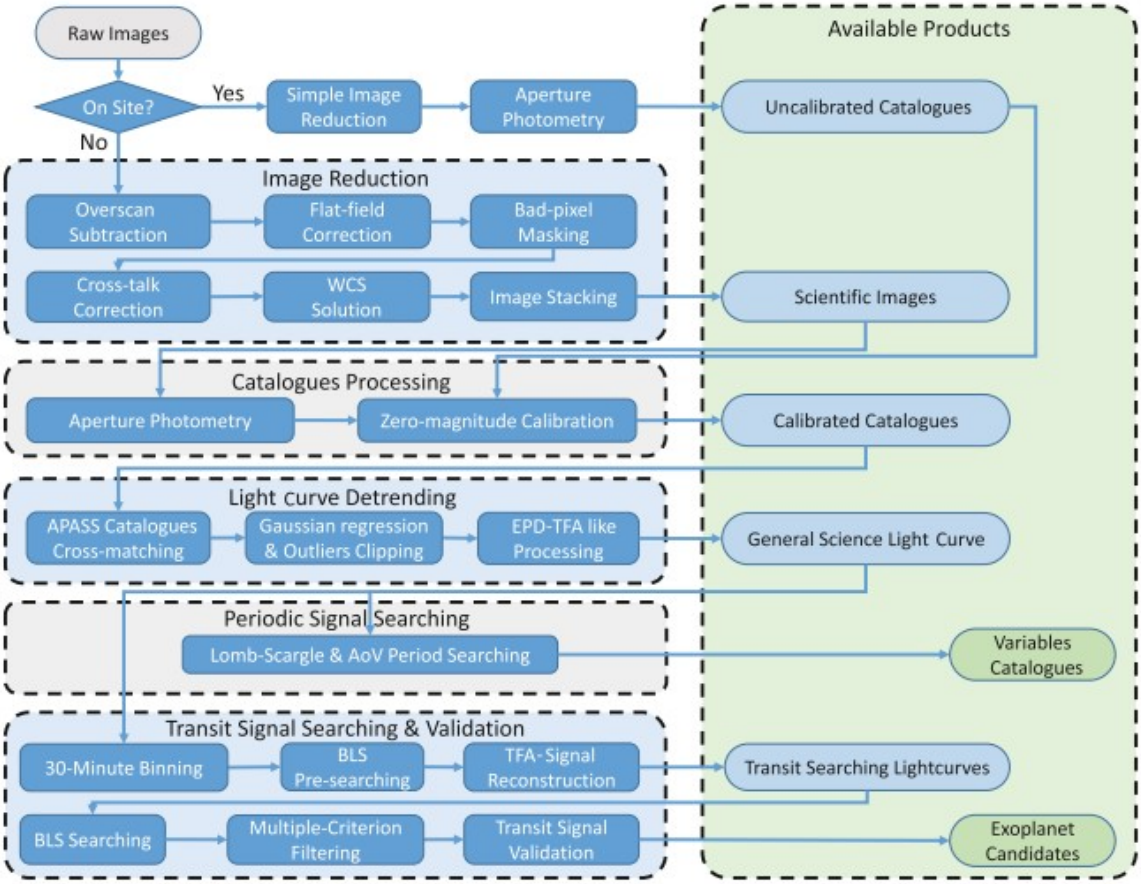

Figure 5. Data reduction flowchart of the exoplanet searching project using the AST3 telescopes.

4.1. Image Reduction

The image reduction component includes some standard steps (e.g., overscan subtraction, dark-current subtraction, and flat-field correction), as well as some special steps to correct specific features within our data (e.g., cross-talk effects and electromagnetic fringes).

4.1.1. Overscan Subtraction

As shown in Figure 1, the 10K × 10K STA1600FT CCD camera installed on AST3-II works in a frame transfer mode and produces an image size of

12,000 × 5300, including overscan regions. At both the top and the bottom boundaries, there are 60 rows that are insensitive to light; these are trimmed off before further reductions. The rest of the image is divided into 16 readout channels, with eight at the top and eight at the bottom. The vertical readout direction of the channels at the top or bottom of an image is from the center to the top or bottom, respectively. The horizontal readout direction is always from left to right within each channel. Within a readout channel, the first 10 rows and the last 180 columns compose a reverse "L"-shaped overscan region surrounding the photosensitive area, which has a size of 1320 × 2580 pixels. Instead of simple bias subtraction, we perform a 2D overscan subtraction for each channel: horizontal subtraction first and then vertical subtraction. Taking a top channel as an example, its horizontal overscan region is located at its bottom. This region, which is composed of 10 rows and 1500 columns, is median combined to a single row, and this combined row is fitted using a second-order polynomial function and subtracted from the other 1320 rows (including the vertical overscan region). Then, the vertical overscan region at the right, which is now 1320 rows by 180 columns, is median combined, second-order polynomial fitted, and subtracted from each column of the final photosensitive area. The channels at the bottom are then processed in a vertically flipped direction. After the 2D overscan subtraction, the photosensitive areas of all the channels are fitted together to form a new image (see Figure 6).

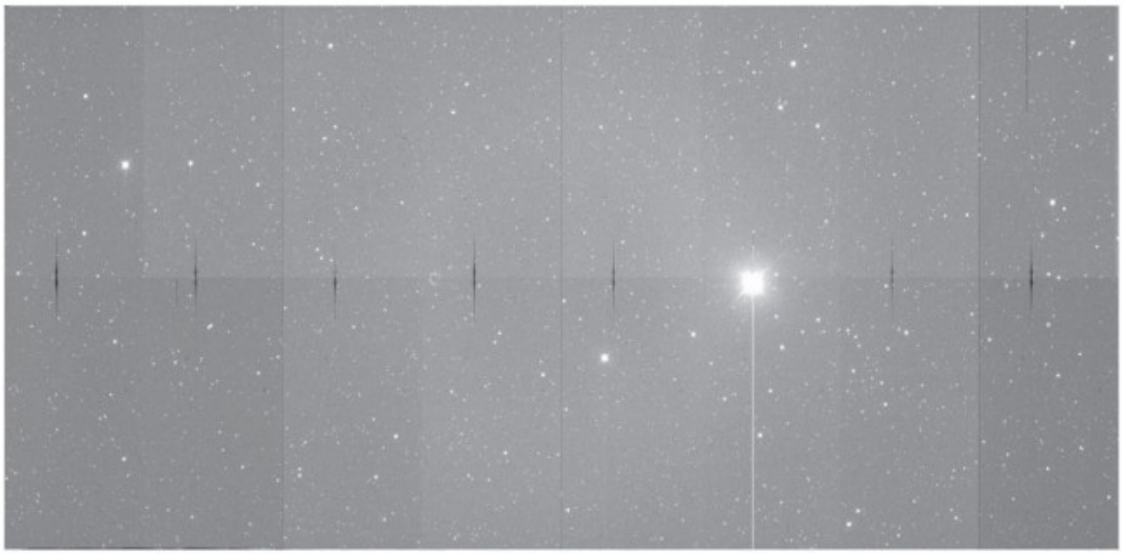

Figure 6. Overscan-subtracted image. The dark vertically extended spots are caused by cross-talk from the highly saturated star.

4.1.2. Cross-talk Correction

In the overscan-subtracted image, serious dark spots can be seen at the same positions along the readout direction in each channel (see Figure 6). These are the cross-talk effects caused by saturated stars in other channels. When one amplifier is reading out a saturated pixel, the video signal can contaminate the pixel streams that are being read out simultaneously from

the other amplifiers. In the AST3-II images, the cross-talk effects appear as negative ghosts of their saturated source stars. The depth of such a ghost is several tens of ADUs below the sky background and varies from channel to channel. Since there are 16 readout amplifiers in our CCD camera, these cross-talk effects are significant. Each saturated star results in 15 negative ghosts in the other 15 readout channels, and any real stars at the positions of these ghosts are made to appear artificially faint. A detailed discussion of the causes of this cross-talk is beyond the scope of this work. Here we only describe how we eliminate its influence from our data. The basic idea can be summarized in the following steps.

1. Mark all saturated pixels (by setting the value of unsaturated pixels as 0) in every readout channel and combine all channels into a single template channel (flipping the top channels vertically) that reflects the positions of all of the saturated stars/pixels in the entire image.

2. Redistribute this template channel into all 16 channels (flipping the top channels vertically) to produce a copy of the original image showing the locations of all of the ghosts.

3. Find the difference between the bottom of each ghost spot and the local sky background, then add this back to the pixels inside the spot. Repeat this process for every readout channel.

However, there are some complicating factors. First, some ghosts may overlap with each other, and the overlapped region is darkened twice. Second, a saturated star always generates a halo that also causes cross-talk, even if the halo itself is not saturated. Thus, the corresponding ghost may have a halo, and this halo region may escape from the very first marking step (which marks only saturated pixels). As a result, every ghost has its own structure, and the depth within a ghost is not constant. Finally, the gains of amplifiers are different from channel to channel. So the depths of the ghosts caused by the same saturated star are different in different channels. The depths of the ghosts within the same channel but caused by sources in different channels are different as well. To solve these problems, we decompose each ghost into three parts: the core region, which is caused by the saturated star itself; the halo region, which is caused by charge bleed from the saturated star; and the overlapped region of two or more saturated stars. The pixels within the halo region are not saturated but contain extra charge due to charge-bleed issues caused by the neighboring saturated pixels. The template channel is also decomposed into three corresponding layers (see the captions of panels (a)–(d) in Figure 7 for more details.). Within each layer, we identify all connected pixels and group them as a "subghost." This is similar to identifying stars within an image when performing photometry. We then redistribute each layer into all 16 channels to show the locations of all "subghosts" in the original image. Finally, we examine every identified "subghost," fit its median depth, and add it back to the pixels affected by this "subghost" in the original image. This process is repeated for

all readout channels. Figure 8 shows the result of our cross-talk correction. Darkening caused by the cross-talk effects is reduced and less than the variation of the local sky background in the corrected image.

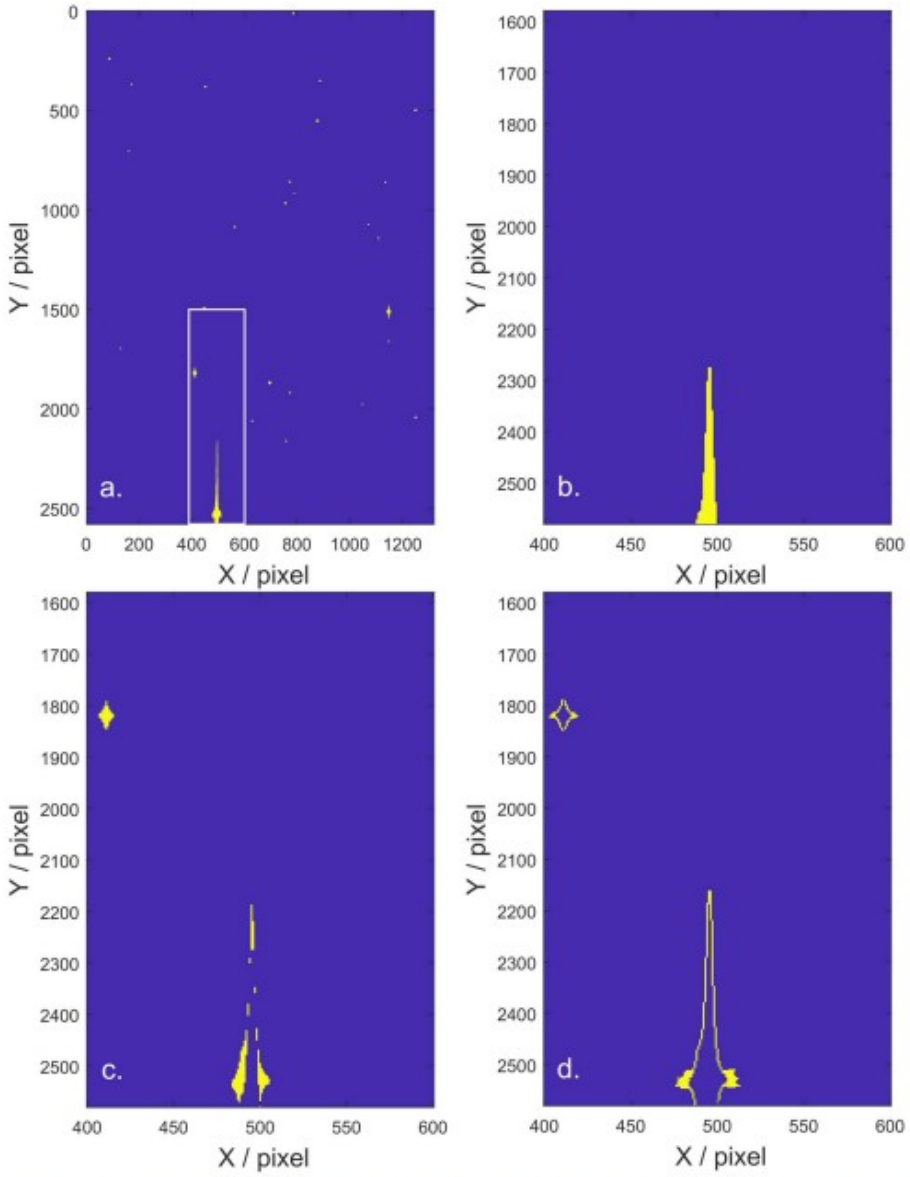

Figure 7. Panel (a): template channel of cross-talk effects. This is a binary map with cross-talk-affected pixels marked as bright yellow and other pixels marked as dark blue. Each starlike spot in this template is produced by a saturated star lying in one of the 16 readout channels. It shows the local positions of the darkened spot (which is also called the ghost of a saturated star) in each of the other 15 channels. This template channel is then copied 16 times and grouped as the formation of the original image (eight columns × two rows) to generate a completed map that marks all the pixels affected by the cross-talk effects. With this map, we can simply mask all of these unreliable pixels, or try to reduce the cross-talk effects down to a level less than the variation of the local sky background. The latter choice requires a detailed structure of the darkened area. This is done by decomposing this template into three layers. For better illustration, we zoom in around two ghosts (enclosed by the white box) and show the layers of the overlapped, core, and halo regions in panels (b)–(d), respectively. Panel (b): The bright yellow pixels show the overlapped region of two ghosts caused by two saturated stars lying in similar positions of different channels. Note that the overlapped region does not necessarily exist in every ghost; the one on the top left has no such overlapped region. Panel (c): The bright yellow region shows the nonoverlapped parts of the core regions of the two ghosts. Note that only nonoverlapping saturated pixels are included in the core region. Panel (d): The halo region of each ghost is shown in bright yellow. These pixels are not saturated but are affected by the charge-bleed issues.

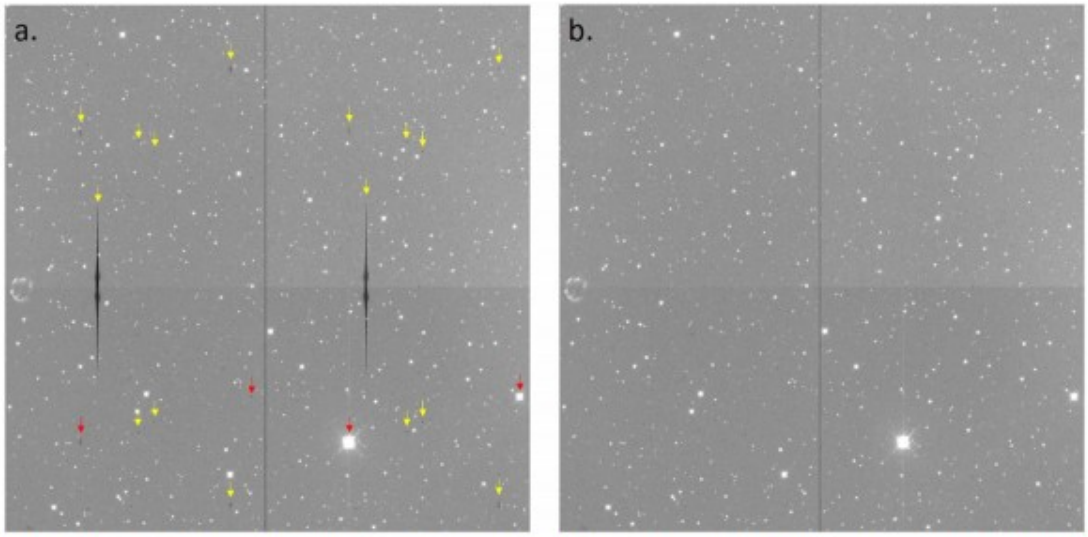

Figure 8. Result of our cross-talk correction. Panel (a): the central part of an image, which consists of four corners from four channels. The dark spots/ghosts marked by yellow arrows are caused by the cross-talk effects. Note that their positions are the same in different channels. Red arrows mark two ghosts and their sources. Panel (b): the same region after cross-talk correction. The darkening caused by the cross-talk effect has been reduced down below the variation of the local sky background.

4.1.3. Flat-field Correction

During twilight periods before the polar winter in 2016, hundreds of twilight-sky images were taken. These twilight images are combined to produce the master flat field. Owing to the relatively large FOV of 4.3 deg^2, a sky brightness gradient of ~1%–10% remains in individual twilight images after preprocessing for cross-talk, overscan, and dark current (for a detailed treatment of dark current, see Ma et al. 2014). Two hundred twilight images were selected to model this sky brightness gradient. For each of the selected images, the brightness gradient was first fitted with an empirical function based on the Sun's altitude and position angle. Then, the fitted gradient was divided from each twilight image, and the resulting 200 twilight images were median combined to produce a master flat field. The final flat-field error is well below 1%. More details of the brightness gradient model and uncertainties in the flat field can be found in Wei et al. (2014).

4.1.4. Electromagnetic Interference Correction

Another feature of our CCD images is electromagnetic interference. Straight and inclined fringes can be easily identified in each channel (see panel (a) in Figure 9). The inclined angles are different in the top and bottom halves of each image; thus, a series of "<"-shaped fringes are formed and spread across the entire image. Pixels affected by these fringes will be brightened or darkened by about 20–50 ADU, which has to be corrected before we can achieve millimagnitude precision. These interference fringes are thought to be caused by noise from the camera's power supply being electrically and/or magnetically coupled into the CCD readout signal chain (though this has not yet be confirmed). The best way to remove this noise would be at the source by improving the grounding and shielding of the entire power supply system. In the absence of such a solution, we model the positions and influences of

each noise fringe and correct them in software. However, this has turned out not to be easy. While the pattern of the fringes remains very similar, they move across the image with time. So, the affected pixels and impact on them vary from frame to frame. Even within a single fringe, only a fraction of the pixels are affected, and the amplitudes of the affected pixels also vary. It is very difficult to identify the affected pixels, especially those that are also overlapped by stars. Our adopted solution is not yet ideal, but it is simple. We take three 10 s exposures for the same field, resample, and match the last two frames to the first one to guarantee pixel alignments. Finally, all three pixel-aligned images are median combined by the Swarp code (Bertin et al. 2002) to produce a new image with lower background variation (Zackay & Ofek 2017). Since the fringe pattern is moving, a pixel is usually affected in only a single frame of the three. Therefore, the median combination may have a good chance to reject the polluted value as an outlier and reveal the real sky background. This simple process helps to reduce the influence of the fringe noise to an acceptable level. A comparison of images before and after stacking is presented in Figure 9.

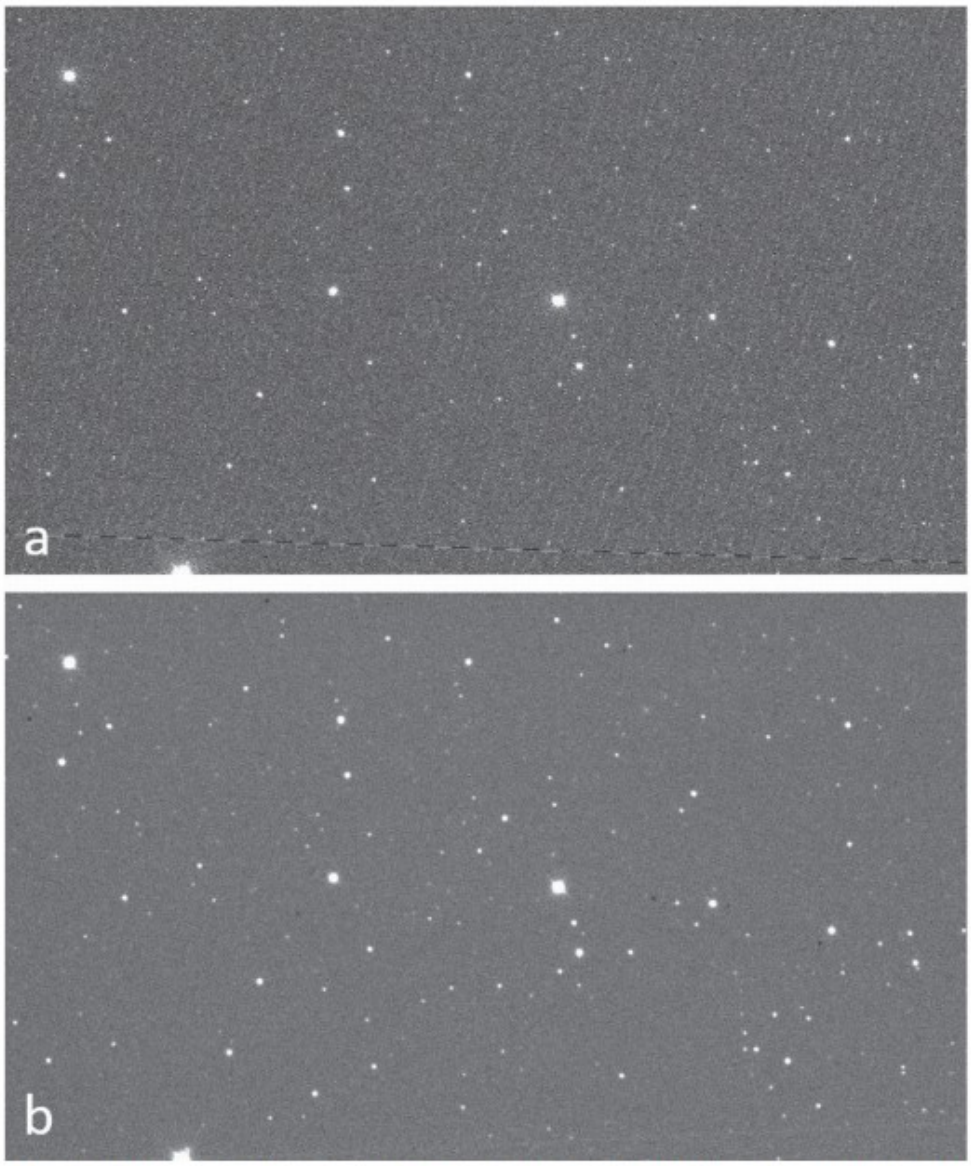

Figure 9. Electromagnetic interference correction. In panel (a), strong fringes can be seen across the whole image. In panel (b), after coadded stacking of three adjacent frames, the relative intensity of the fringes is reduced.

4.2. Photometry and Calibration

The cleaned images from the preceding steps are then registered and coadded by Astrometry.net (Lang et al. 2010) and Swarp (Bertin et al. 2002), respectively. As we mentioned above, the cadence of stacked images is about 12 minutes with an effective exposure time of ~30 s. These images are labeled as "scientific images" and are a major component of our data products. Aperture photometry is then performed on these scientific images, and star catalogs are generated using Sextractor (Bertin & Arnouts 1996). For each image, the total photometry process is divided into two steps. First, we output a simple catalog that contains only the positions and fluxes using optimal apertures (corresponding to the keyword FLUX_AUTO). This simple catalog is then cross-matched with the AAVSO Photometric All-Sky Survey

(APASS) catalog (which is conducted in five filters: the Johnson *B* and *V* and Sloan *g*, *r*, and *i* bands; Henden et al. 2015). The *i*-band magnitudes and fluxes of all matched stars are extracted from the APASS and AST3 catalogs, respectively. The zero-point magnitude is then fitted from the power-law relation of magnitude and flux (Figure 10). Second, we adopt the fitted zero-point magnitude and run Sextractor again to produce the final calibrated catalog. Although we use a Sloan *i*-band filter, there may be some systematic offsets or color dependences between our results and that from the APASS database. The major sources may include the manufacturing difference between our filter and the one adopted by APASS, the absence of a strong water feature in the *i* band due to the extremely low water vapor in Antarctica, and the differences in the magnitude cutoff and colors of the different ensembles of reference stars. To demonstrate these issues, we fit a simple relation, $\Delta m_i = m_{i,\mathrm{ast3}} - m_{i,\mathrm{apass}} = c(m_r - m_i)_{\mathrm{apass}} + b$, in each field to show the color dependence of our magnitude calibration. Here $c \equiv d\Delta m_i / d(m_r - m_i)$ is the slope of the color dependence and *b* is a magnitude offset. Results from our 10 target fields are shown in Figure 11. The fitted slope and uncertainty of the color dependence in each field is also labeled in each panel. We find a median value of the slope, $c_{\mathrm{median}} = -0.0771$, among all 10 target fields. The slopes of the color term are close to zero in all target fields, which indicates that the color issue is insignificant within our result. However, it is still worth noting that this color term has not been corrected in this data release, and it will be considered in future data releases.

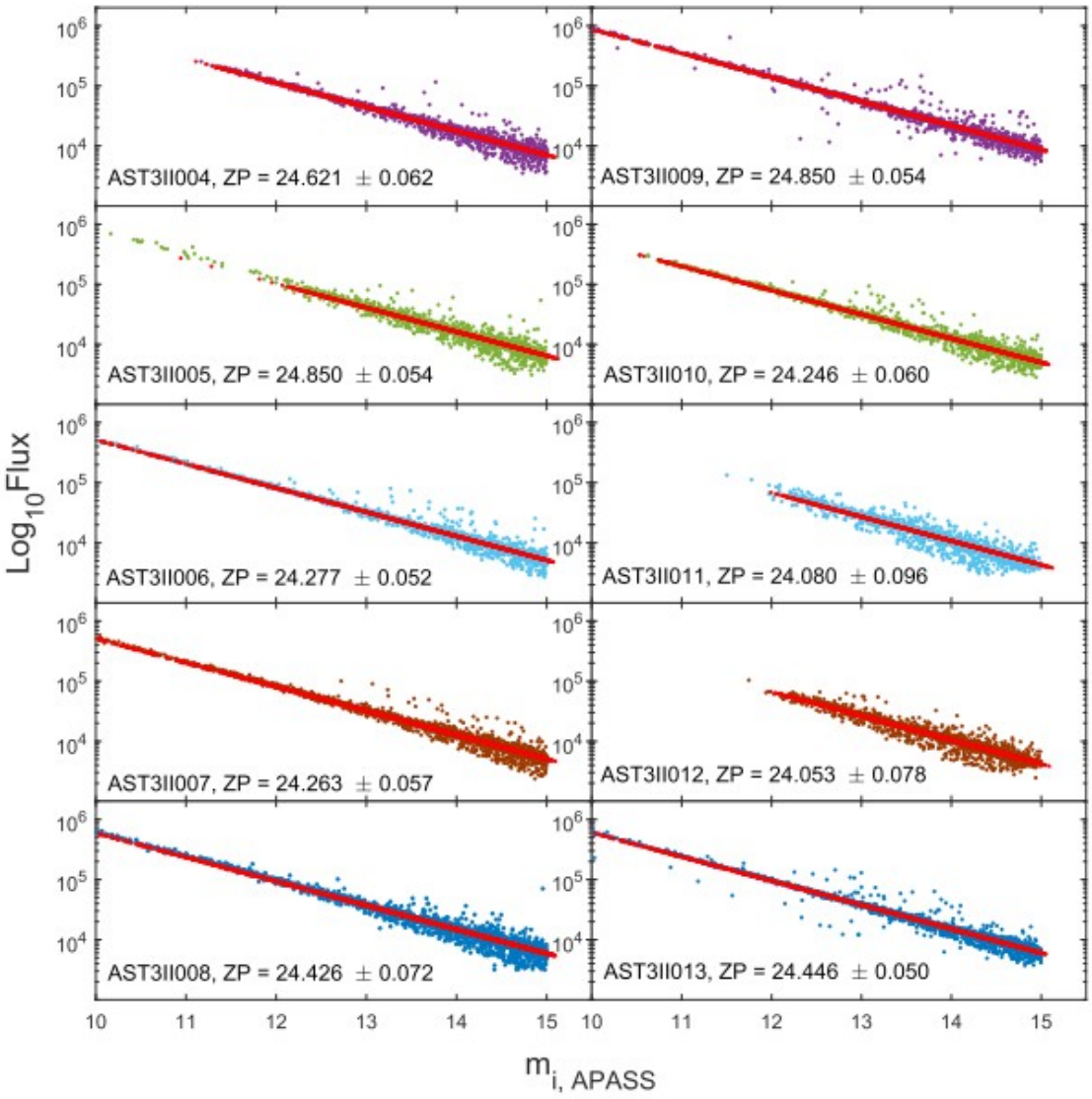

Figure 10. Fitted zero-point magnitude (i_{zp}) in the Sloan i band for each target field. The y axis is the logarithmic flux (logF) measured by the AST3-II, and the x axis is the i-band magnitude (i_{apass}) in APASS. The solid red line shows the fitting result of this relation: $i_{apass} = i_{zp} - 2.5$ logF.

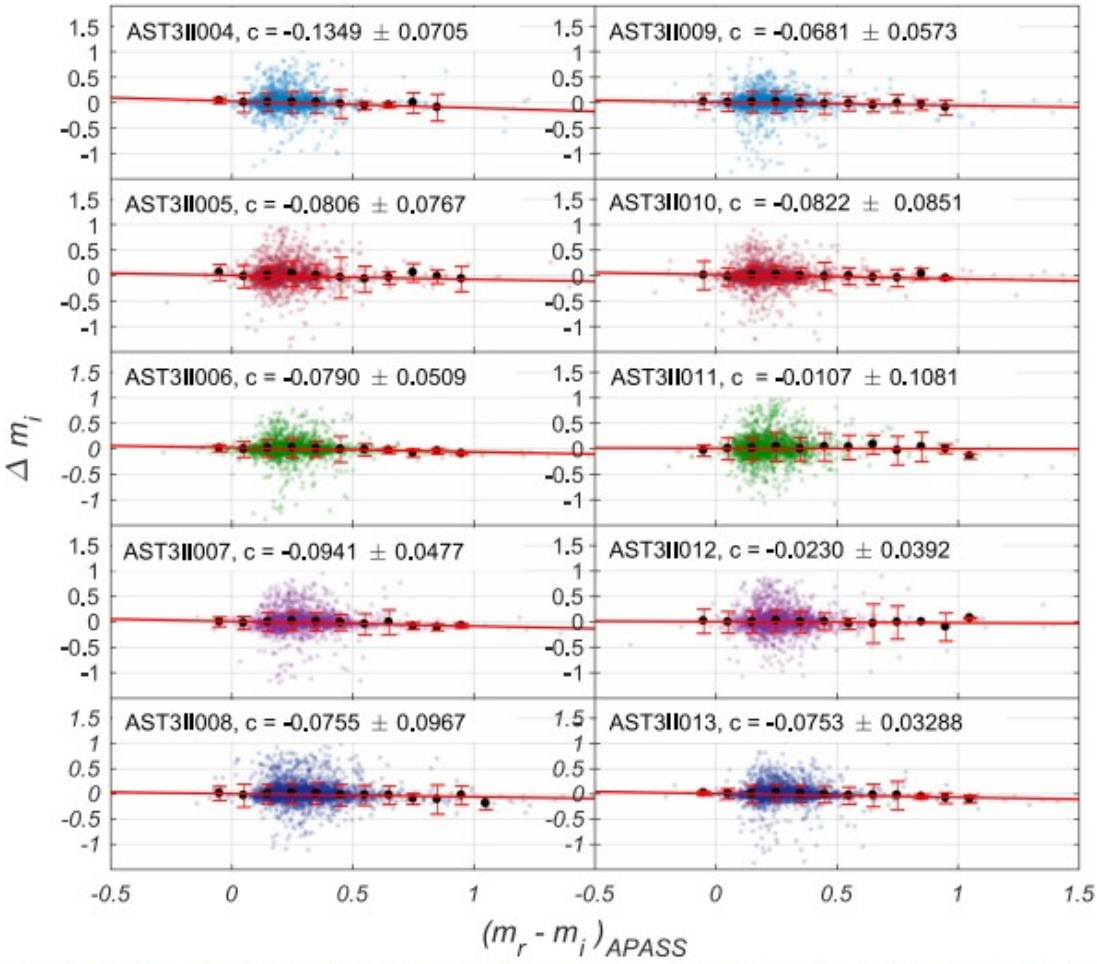

Figure 11. Color dependence of magnitude calibration in each target field. Here we demonstrate the relation between Δm_i, the difference between the calibrated i magnitude and the corresponding i magnitude in the APASS catalog, and the color term in APASS ($m_r - m_i$). The filled black circles are median-binned Δm_i with a color interval of 0.1. Only those stars brighter than $m_i = 12$ are adopted to produce median bins. The error bar of each bin shows the rms of measurements within each interval. The color dependence is linearly fitted to these bins and shown by a solid red line in each field. The fitted slope of the color dependence of each field is also labeled in each panel.

In the calibrated catalog, we output image positions, J2000.0 equatorial coordinates and their variances, photometry results of optimal aperture and three fixed apertures (8, 10, and 12 pixels, which are, according to our plate scale, 8'', 10'', and 12'', respectively), parameters listing observation conditions, and parameters from image statistics. All of these pieces of information are inherited by the light curves and used as external trend parameters in the following light-curve detrending process. An example of a catalog header is shown in Table 2.

Table 2
An Example Catalog Header of an Image Taken on "2016–05–03T16:34:44.34."

Name	Example/Description	Units
Observation start time	2016–05–03T16:34:44.34	UT
Exposure time	30	s
CCD temperature	217.92	K
Airmass	1.07	mag
Solar altitude	−23.87	deg
Moon distance	90.82	deg
Zero-point mag	21.93	mag
# 1 XWIN_IMAGE[a]	Image position in x axis	pixel
# 2 YWIN_IMAGE	Image position in y axis	pixel
# 3 X2WIN_IMAGE	Position variance in x axis	pixel^2
# 4 Y2WIN_IMAGE	Position variance in y axis	pixel^2
# 5 XYWIN_IMAGE	Position covariance between x and y axis	pixel^2
# 6 ERRX2WIN_IMAGE	Error of position variance in x axis	pixel^2
# 7 ERRY2WIN_IMAGE	Error of position variance in x axis	pixel^2
# 8 ERRXYWIN_IMAGE	Error of position covariance between x and y axis	pixel^2
# 9 CXXWIN_IMAGE[b]	First ellipse parameter of object's isophotal shape	pixel^{-2}
# 10 CYYWIN_IMAGE	Second ellipse parameter of object's isophotal shape	pixel^{-2}
# 11 CXYWIN_IMAGE	Third ellipse parameter of object's isophotal shape	pixel^{-2}
# 12 XWIN_WORLD	R.A. in J2000.0	deg
# 13 YWIN_WORLD	Decl. in J2000.0	deg
# 14 ERRX2WIN_WORLD	Error of position variance in R.A.	deg^2
# 15 ERRY2WIN_WORLD	Error of position variance in decl.	deg^2
# 16 ERRXYWIN_WORLD	Error of position covariance between R.A. and decl.	deg^2
# 17 MAG_AUTO	Kron-like elliptical aperture magnitude	mag
# 18 MAGERR_AUTO	rms error for AUTO magnitude	mag
# 19 FLUX_AUTO	Flux within a Kron-like elliptical aperture	count
# 20 FLUXERR_AUTO	rms error for AUTO flux	count
# 21 MAG_APER	Fixed-aperture magnitude vector	mag
# 24 MAGERR_APER	rms error vector for fixed-aperture mag	mag
# 27 FLUX_APER	Flux vector within fixed circular aperture(s)	count
# 30 FLUXERR_APER	rms error vector for aperture flux(es)	count
# 33 FWHM_IMAGE	FWHM assuming a Gaussian core	pixel
# 34 ELONGATION	Ellipticity of object's isophotal shape	...
# 35 BACKGROUND	Background at centroid position	count
# 36 THRESHOLD	Detection threshold above background	count
# 37 FLUX_RADIUS	Fraction-of-light radius	pixel
# 38 FLAGS[c]	Extraction flags	...

Notes. Position- and flux-related measurements (keywords) are generated by Sextractor (Bertin & Arnouts 1996).
[a] All position-related measurements, e.g., XWIN_IMAGE, XWIN_WORLD, etc., are performed through a Gaussian window function, i.e., the centroid coordinates are calculated through an iterative process updated by a Gaussian-weighted integration of the coordinates of isophotal pixels. The start point is set to be the first-order moment of the source. More details can be found in Bertin & Arnouts (1996). All "Windowed" measurements are denoted with a "WIN," "_IMAGE" means in pixel coordinates, and "_WORLD" means in equatorial coordinates.
[b] CXXWIN_IMAGE, CYYWIN_IMAGE, and CXYWIN_IMAGE are three ellipse parameters describing the shape of an object's isophotal ellipse. $\text{CXXWIN\_IMAGE}(x-\bar{x})^2 + \text{CYYWIN\_IMAGE}\,(y-\bar{y})^2 + \text{CXYWIN\_IMAGE}\,(x-\bar{x})(y-\bar{y}) = R^2$, where x and y are XWIN_IMAGE and YWIN_IMAGE, and $\bar{x}$ and $\bar{y}$ are mean values of XWIN_IMAGE and YWIN_IMAGE, respectively. The last constant $R = 3$.
[c] FLAGS contains, coded in decimal, all the extraction flags as a sum of powers of 2. 1: The object has neighbors bright and close enough to significantly bias the MAG_AUTO photometry or bad pixels (more than 10% of the integrated area affected). 2: The object was originally blended with another one. 4: At least one pixel of the object is saturated (or very close to). 8: The object is truncated (too close to an image boundary). 16: Object aperture data are incomplete or corrupted. For example, an object close to an image border may have FLAGS = 16 and perhaps $\text{FLAGS} = 2 + 4 + 8 + 16 = 30$.

4.3. Light-curve Detrending

The general concept behind our light-curve "polishing" process is to perform blind detrending that removes the common variations among all targets. Two such methods have been commonly employed in data reduction for wide-field photometric surveys: systematic effects remove (SYSREM; Tamuz et al. 2005) and trend-filtering algorithm (TFA; Kovács et al. 2005). We implemented a TFA-like algorithm with some minor adjustments. First, the reference stars of a target light curve were selected according to their distances to the target star (e.g., they must be in the same readout channel as the target star). Second, we built an individual trend matrix (whose columns are magnitudes of reference stars and external parameters) for

each target light curve and updated it dynamically according to the correlation coefficients between the brightness variations of the target and its reference stars. Those stars with large variations were then clipped from the reference star list after iteration. Third, the external parameters of the target star, e.g., its airmass, distance to the moon, FWHM, local background variation, etc. (see Table 3 for details), were recorded simultaneously with the brightness measurements and are now appended to its trend matrix as additional columns. The variations present in these external parameters will be used to detrend the target light curve. This is usually called the EPD process. Here we combine the EPD- and TFA-like processes together and detrend the target light curve using its external parameters and brightness of reference stars simultaneously. Finally, instead of the least-squares fit to the linear combination of the reference light curves in the standard version of TFA, the detrending process in our pipeline is achieved by a multivariable linear regression with each column in the trend matrix marked as a "variable." We noticed that some outliers, caused by mismatches of stars or bad weather, caused serious problems in the detrending processes, and occasionally they may crash the box least-squares (BLS) fitting searching function that follows. To eliminate these outliers and retain large physical variations at the same time, we performed a Gaussian regression to model the time-dependent variations within each light curve, and we then clipped all measurements that are more than 3σ away from the model before using them in the detrending process.

Table 3
Columns in Raw Light Curves

Column No.	Name	Explanation	Units
1	Time	AST3 observation time in UT (JD—2,456,000)	day
2	XWIN_IMAGE	Image position in x axis	pixel
3	YWIN_IMAGE	Image position in y axis	pixel
4	X2WIN_IMAGE	Position variance in x axis	pixel^2
5	Y2WIN_IMAGE	Position variance in y axis	pixel^2
6	XYWIN_IMAGE	Position covariance between x and y axis	pixel^2
7	ERRX2WIN_IMAGE	Error of position variance in x axis	pixel^2
8	ERRY2WIN_IMAGE	Error of position variance in y axis	pixel^2
9	ERRXYWIN_IMAGE	Error of position covariance between x and y axis	pixel^2
10	CXXWIN_IMAGE	First ellipse parameter of object's isophotal shape	pixel^{-2}
11	CYYWIN_IMAGE	Second ellipse parameter of object's isophotal shape	pixel^{-2}
12	CXYWIN_IMAGE	Third ellipse parameter of object's isophotal shape	pixel^{-2}
13	XWIN_WORLD	R.A. in J2000.0	deg
14	YWIN_WORLD	decl. in J2000.0	deg
15	ERRX2WIN_WORLD	Error of position variance in R.A.	deg^2
16	ERRY2WIN_WORLD	Error of position variance in decl.	deg^2
17	ERRXYWIN_WORLD	Error of position covariance between R.A. and decl.	deg^2
18	MAG_AUTO	Kron-like elliptical aperture magnitude	mag
19	MAGERR_AUTO	rms error for AUTO magnitude	mag
20	FLUX_AUTO	Flux within a Kron-like elliptical aperture	count
21	FLUXERR_AUTO	rms error for AUTO flux	count
22–24	MAG_APER	Fixed-aperture magnitude vector	mag
25–27	MAGERR_APER	rms error vector for fixed-aperture mag.	mag
28–30	FLUX_APER	Flux vector within fixed circular aperture(s)	count
31–33	FLUXERR_APER	rms error vector for aperture flux(es)	count
34	FWHM_IMAGE	FWHM assuming a Gaussian core	pixel
35	ELONGATION	Ellipticity of object's isophotal shape	...
36	BACKGROUND	Background at centroid position	count
37	THRESHOLD	Detection threshold above background	count
38	FLUX_RADIUS	Fraction-of-light radius	pixel
39	FLAGS	Extraction flags	...
40	exposure_time	Exposure time	s
41	CCD_temperature	Temperature of CCD chip	K
42	airmass	Airmass	...
43	Sun_altitude	Altitude of the Sun	deg
44	moon_distance	Angular distance to the Moon	deg
45	zeropoint	Zero-point magnitude	mag

Note.
Keywords have the same meaning as in Table 2.

In this data release, we present two versions of light curves for general science usage: the raw light curves that contain all the original information (see Table 3) and the detrended light curves that contain only time, magnitude, and the error in the magnitude. The cadence of these light curves is ~12 minutes, and the best rms after detrending is ~4 mmag at the bright end, $m_i = 10$. This precision is good enough to search binaries or pulsating variables; however, to search for transiting exoplanets, we need higher precision. To achieve this, the light curves are then further "polished" and binned to 36 minutes, after which they achieve a best rms of 2 mmag at $m_i = 10$ (see Figure 12). The curves of the expected photon-limited rms against magnitude are also overplotted in Figure 12. Note that when we calculate the photon noise, the sky background noise, readout noise, saturation limit, and average number of measurements falling in the binned intervals are also considered. As a result, the photon limit of light curves with a 36 minute cadence is not simply improved by a factor of $\sqrt{3}$ but rather a factor of $\sim\sqrt{2}$, to that of a 12 minute cadence. The rms of the binned light curves is improved a lot at the bright end; however, there are still hidden systematic errors that prevent us from reaching the photon-limited precision.

The detrending process and further polishing determine the final precision of our light curves and directly influence the detection rate of transit signals. The detailed algorithm and parameter settings, e.g., the number of reference stars and selection of external parameters, will be presented in a following paper (Zhang et al. 2018) that concentrateson transiting exoplanet searching.

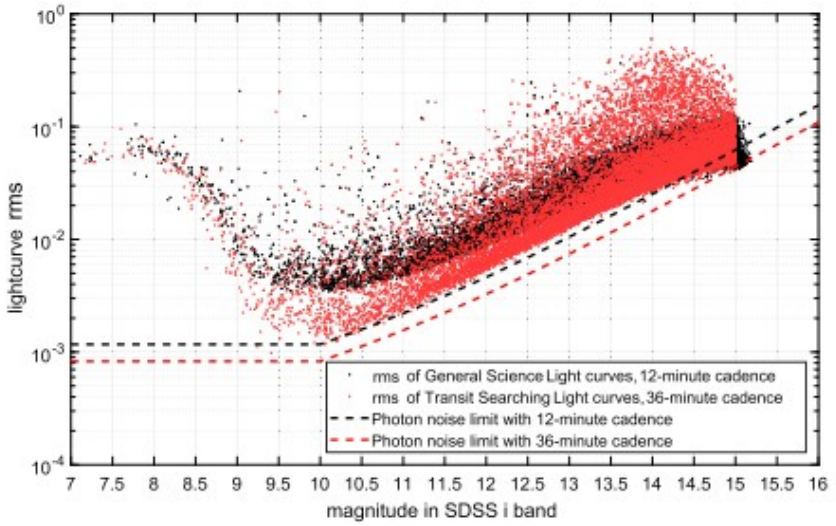

Figure 12. Light-curve rms vs. magnitude of 26,578 stars. Each point represents the overall rms of a detrended light curve with time spanning the whole observation campaign. The black points are light curves with a cadence of ~12 minutes, and the red ones are light curves binned to 36 minutes. The expected photon limits (black dashed line for 12 minute cadence and red dashed line for 36 minute cadence) against magnitude are also overplotted. Note that when we calculate the photon noise, the sky background noise, readout noise, saturation limit, and average number of measurements falling in the binned interval are also considered. So the photon limit of the 36 minute cadence is not simply improved by a factor of $\sqrt{3}$ but a rather a factor of $\sim\sqrt{2}$, to that of the 12 minute cadence. Stars brighter than $m_i = 10$ are likely to be saturated and suffer large variations. However, we still found some obvious variables in this magnitude range (see Section 5).

4.4. Periodic Signal Searching

The "L" variability index (Welch & Stetson 1993; Stetson 1996) is used to select potential variable candidates. For each light curve, we calculated its L index using the −Jstet command of VARTOOLS (Hartman & Bakos 2016). The overall distribution of L index in our sample is shown in Figure 13. Two components can be fitted from this distribution, one of which shows a Gaussian profile and corresponds to stars with insignificant variation and the other of which shows an exponential tail and is likely to correspond to variable stars. The intersection of these two profiles is at $L \approx 0.19$. Stars with $L \geq 0.19$ are selected as variable-star candidates and delivered to the "periodic signal-searching" procedure. Periodic and sinusoidal variations are then identified using both the generalized Lomb–Scargle (LS; Press et al. 1992; Zechmeister & Kürster 2009) and the analysis of variance (AoV) (Schwarzenberg-Czerny 1989; Devor 2005) methods. In practice, we integrate the −LS and −aov commands of VARTOOLS into our pipeline. This module produces two data sets from the LS and AoV processes. Periodic signals with S/Ns above 1.5σ in both data sets and above 3σ in single data sets then proceed to visual inspection. Some targets detected by the BLS method (Kovács et al. 2002) in the latter transit signal-searching module, most of which are eclipsing binaries, are also appended to the results of this

module. Only obvious and regular periodic signals that could be classified as binaries or pulsating stars are selected and published in this work. Signals that are classified as rotating spots, rotating ellipsoidal variables, and other semiperiodic/irregular variables will be studied and released in future works.

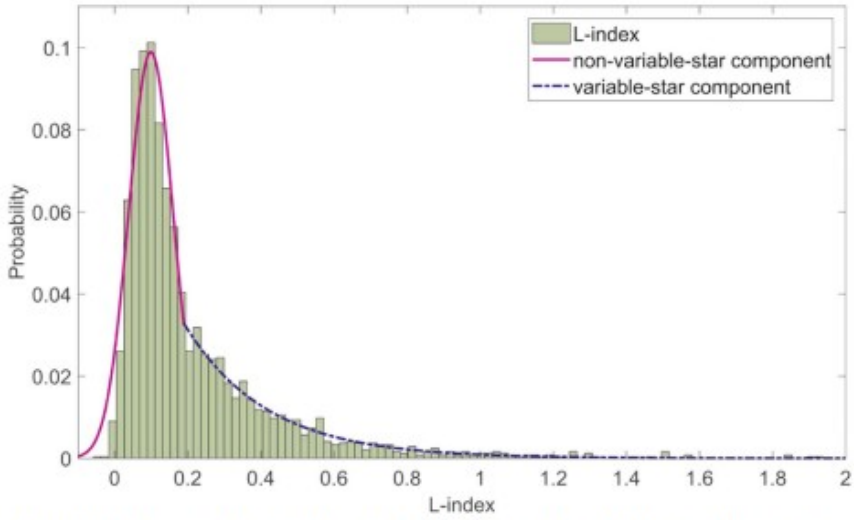

Figure 13. Distribution of the Welch–Stetson variability statistic L for the 26,578 bright stars in the AST3-II data set. Two components can be fitted from this distribution: an exponential profile that corresponds to variable stars and a Gaussian profile that represents stars with insignificant variations.

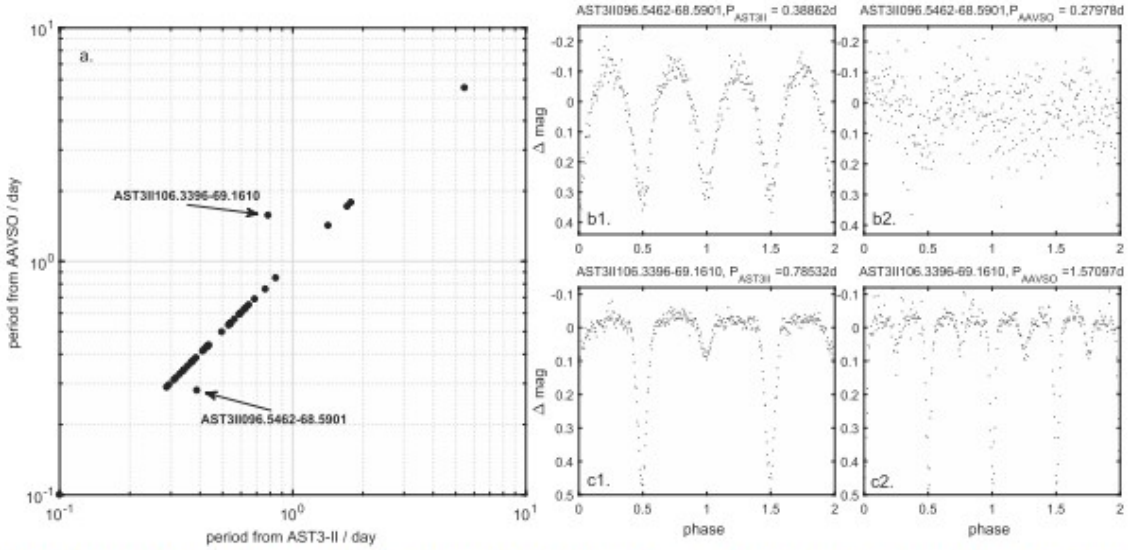

Figure 14. Comparison between the periods of 42 common variables found by AST3-II and present in the AAVSO database. Panel (a): periods from AAVSO vs. periods given in the AAVSO database. There are only two common variables whose periods are not consistent. Panel (b1): phase-folded light curve of target AST3II096.5462-68.5901 according to the period found by AST3-II, $P_{\mathrm{AST3II}} = 0.38862$ days. Panel (b2): phase-folded light curve of target AST3II096.5462-68.5901 according to the period given in the AAVSO database, $P_{\mathrm{AAVSO}} = 0.27978$ days. Panel (c1): phase-folded light curve of target AST3II106.3396-69.1610 according to the period found by AST3-II, $P_{\mathrm{AST3II}} = 0.78532$ days. Panel (c2): phase-folded light curve of target AST3II106.3396-69.1610 according to the period given in the AAVSO database, $P_{\mathrm{AAVSO}} = 1.57097$ days. For both variables, the AST3-II period produces a better result.

To determine the period of a variable that has multiple candidate periods, we fold its light curve with the period found from each of the LS, AoV, and BLS methods and select the one that results in the smallest rms. Then we rerun the corresponding method at a range of ±0.1 days around the selected period with a time step of 0.0001 days. We further fold the light curve

according to the updated period and inspect the plot visually. Confusion is usually caused by some binaries whose primary and secondary eclipses are similar. In this case, the half period often mimics the true period. To distinguish the tiny difference between eclipses, we double the period when we fold the light curve. Therefore, the plot shows the phase from 0.0 to 2.0, and the second phase is not identical to the first one. This ensures that the plot shows two or four deep eclipses, no more and no less (if it has only one or more than four deep eclipses, then we know the original period is wrong; see panels (b1), (b2) and (c1), (c2) in Figure 14), and makes it easier to compare the odd and even eclipses. In most cases, we will find a slight but distinguishable difference between the depth of the odd and even eclipses (e.g., AST3II096.5462-68.5901 in panel (b1) of Figure 14) or a tiny secondary eclipse between two adjacent deep eclipses (e.g., AST3II106.3396-69.1610 in panel (c1) of Figure 14). For contact eclipsing binaries, if the odd and even eclipses are just identical, then we assume the primary and secondary eclipses are both present but indistinguishable and select the period that makes four eclipses from phase 0.0 to 2.0 (e.g., AST3II108.2786-71.7907 in Figure 16). However, for detached eclipsing binaries, if there is no obvious secondary eclipse found, we assume the secondary eclipse is present but undetectable at our precision and select the period that makes two eclipses from phase 0.0 to 2.0 (e.g., AST3II098.1909-70.8216 in Figure 17).

5. Results

We scanned 10 fields within the southern CVZ of *TESS* in the polar nights of 2016. The raw image data acquired by the AST3-II telescope were reduced. Each catalog that is released along with this work is first cross-matched with the APASS point-source catalog in the Sloan *i* band and calibrated by the fitted zero-point magnitude (see Figure 10). The matching radius is set to be 2''. Although we defocused the telescope (FWHM ~ 5'') and adopted a photometry aperture up to 12'', this is no significant blending issue. The reasons are: first, we have to avoid the crowded field, e.g., fields close to the LMC; second, we adopted a short exposure time (10 s), and not too many faint stars were caught; and last, we have a high spatial resolution (pixel scale ~1'' pixel^{-1}), so neighboring targets can be easily distinguished even if they fall in the same aperture. Light curves of stars brighter than 15th magnitude are extracted, detrended (see Figure 12), and released along with this work. From these light curves, we have found 221 variables within the southern CVZ of *TESS*, including 117 binaries and 104 pulsating stars. Their phase-folded light curves are shown in Figures 15–23. Our final variable catalog is cross-matched with the latest AAVSO database and the *TESS* Input Catalog (TIC; Stassun et al. 2018) using a matching radius of 5''. This large matching radius is in consideration of our defocused PSF. In practice, if multiple matches happened within a matching radius, we select the ones with the nearest magnitude. Fortunately, the space distribution of known variables in AAVSO and preselected bright stars in *TESS* is quite sparse. So, no confusion in cross-matching was reported by our matching process. We

list the IDs of matched targets from both the AAVSO database and the TIC in Table 4. The target stellar properties, such as stellar radius, mass, and variable-star type, are also listed. We note that there are 67 targets (identified with a candidate target list (CTL) flag of 1 in Table 4) found in the exoplanet CTL for *TESS*. Targets in the CTL are preselected objects that have higher priorities to search for transiting exoplanets using short-cadence (~2 minutes) light curves. Our detection of variability in these targets indicates that additional care needs to be taken when searching for transit signals in these targets. There are 42 variables in common between our catalog and the AAVSO database. Panel (a) in Figure 14 shows the comparison between the periods of common variables found by AST3-II and in the AAVSO database. There are only two mismatches in period: AST3II096.5462-68.5901 (ASAS J062611-6835.4) and AST3II106.3396-69.1610 (YZ Vol). We plot their phase curves in panels (b1), (b2), (c1), and (c2) according to the periods from AST3-II and the AAVSO database. The periods found from the AST3-II observations (panels (b1) and (c1)) are clearly more convincing.

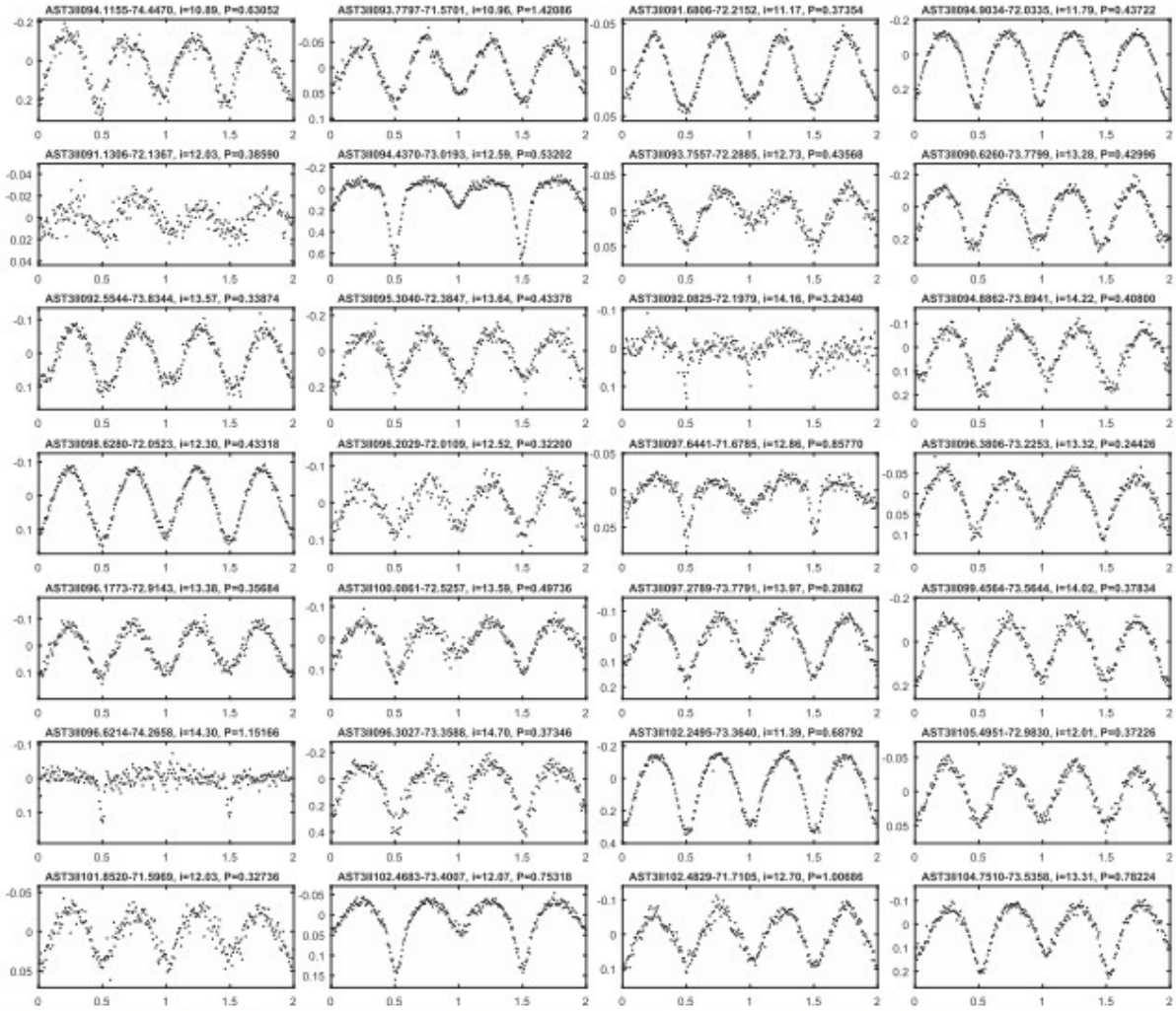

Figure 15. Eclipsing binaries found within the data obtained in 2016 by AST3-II. The label above each panel contains the *i*-band median magnitude (which has been subtracted) for the curves and the period in days. The *x* and *y* axes of each panel are the phases [0, 2] (note that each light curve is folded to two times of its period, so the measurement around phase 1.5 is not identical to that around phase 0.5) and the variation in magnitude Δm_i, respectively.

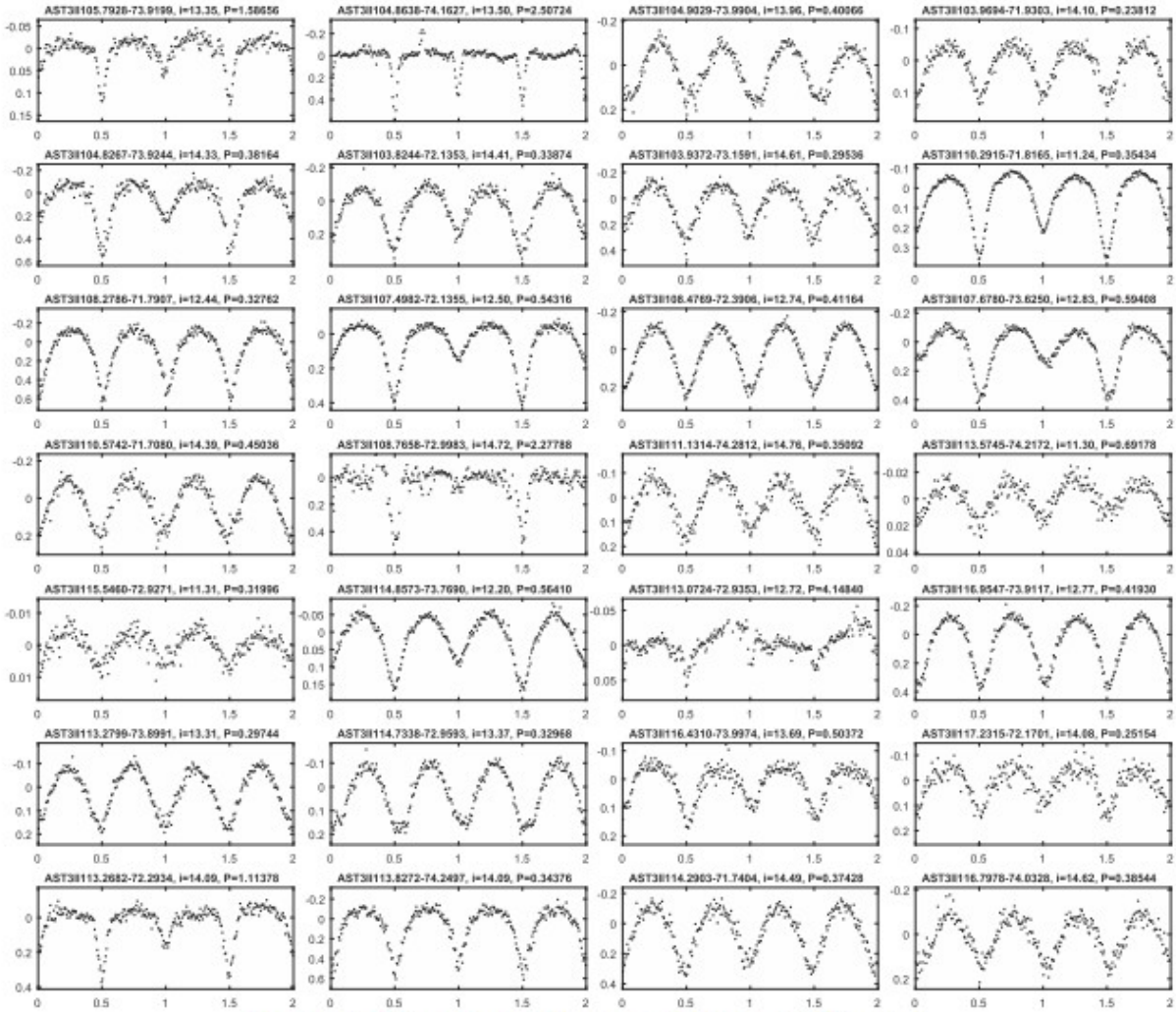

Figure 16. Eclipsing binaries found within the data obtained in 2016 by AST3-II (continued).

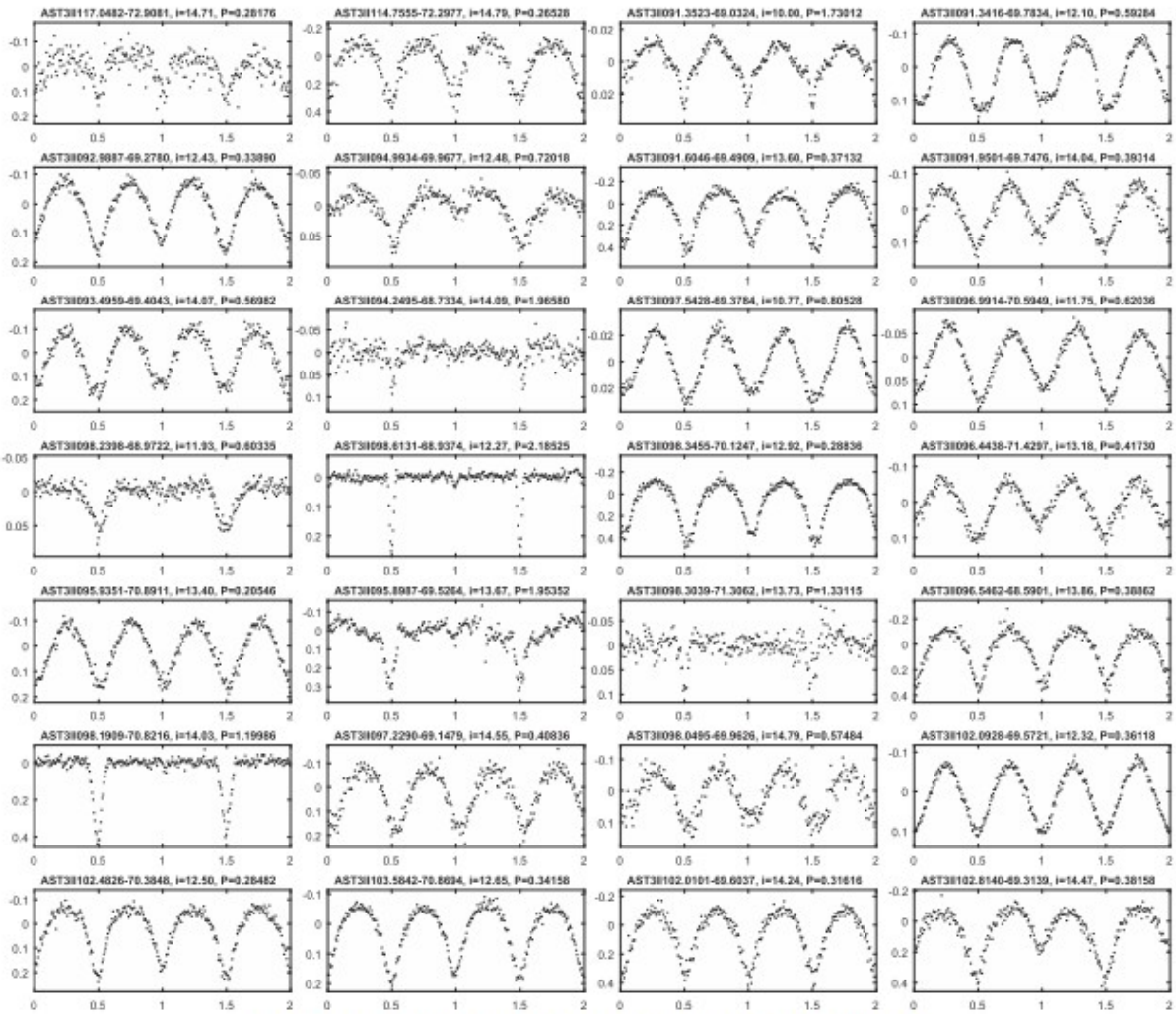

Figure 17. Eclipsing binaries found within the data obtained in 2016 by AST3-II (continued).

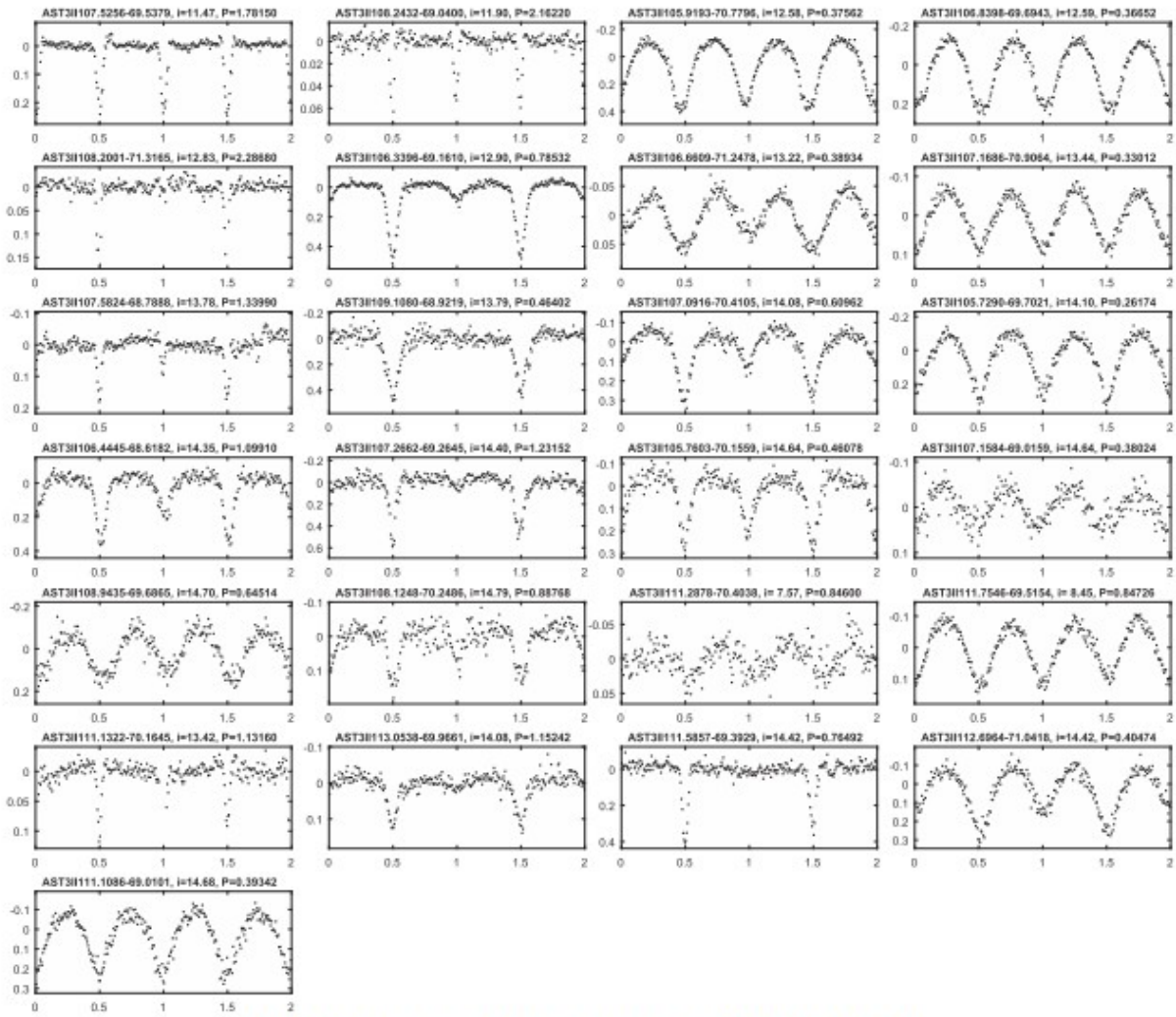

Figure 18. Eclipsing binaries found within the data obtained in 2016 by AST3-II (continued).

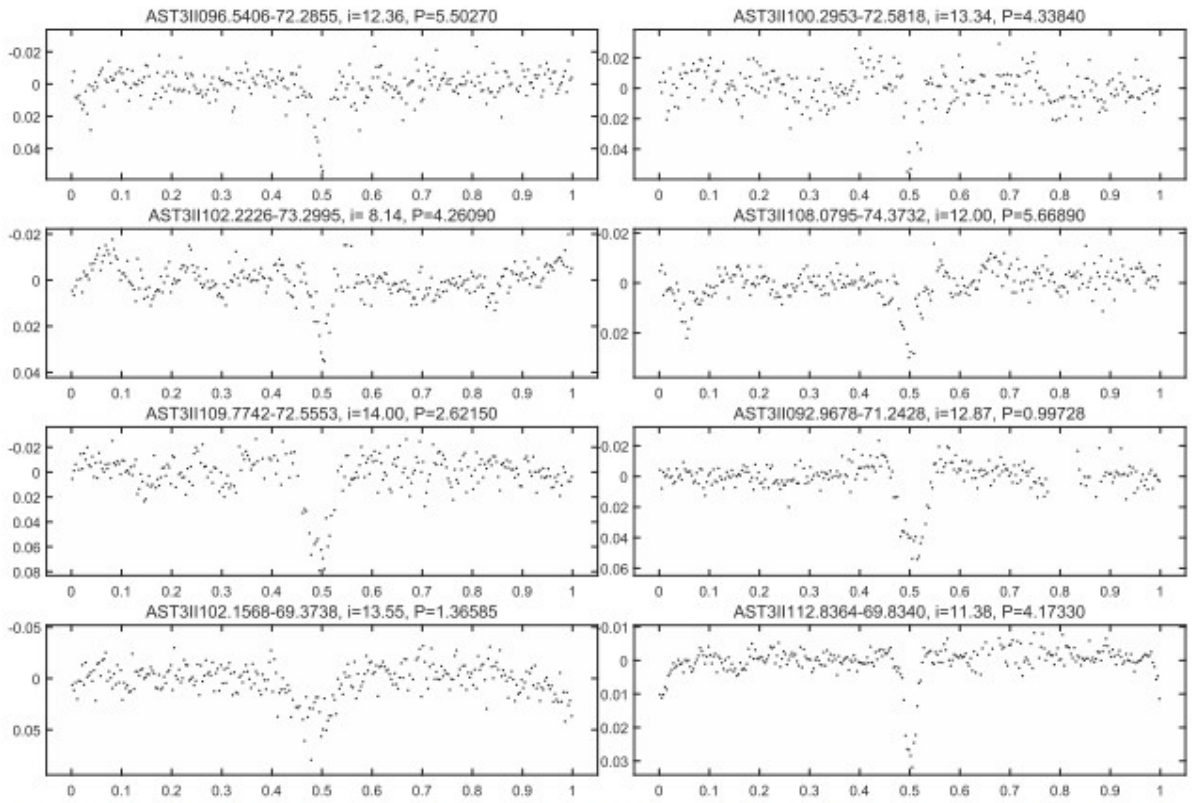

Figure 19. Low-depth eclipsing binaries. We show them separately from the ordinary eclipsing binaries since their depths are less than 5%, and they show insignificant secondary eclipses. These could be easily mistaken for transiting exoplanets if the photometric precision was insufficient to show the sharp "V"-shaped bottom. The *x* and *y* axes of each panel are the phases [0, 1] and the variation in magnitude Δm_i, respectively.

As shown in Figure 12, the valid magnitude range for our survey is from $m_i = 10$ to $m_i = 15$. Most stars brighter than $m_i = 10$ mag are likely to be saturated. However, on occasion, the extinction caused by bad weather or frosting on the front window of the telescope can be as high as 4 mag. During such times of poor photometric conditions, only the brightest stars can be observed, which has the fortunate result that some parts of the light curves of very bright stars ($7.5 < m_i < 10$) are still usable. After filtering out the remaining saturated measurements, the photometric precision from these highly extincted images is sufficient to identify some variables with large periodic variations. For example, target "AST3II111.7546-69.5154" has a magnitude of 8.45 in the *i* band and a variation period of 0.84726 days. It has been labeled as an "EW/KE" variable[26] in the AAVSO database with a variation period of 0.84743 days. Target "AST3II092.1221-71.1200" is 9.09 mag in the *i* band and has a variation period of 1.71539 days. In the AAVSO catalog, its name is "ASAS J060829-7107.2," which is labeled as an "ACV" variable[27] with a period of 1.71443 days.

Another thing worthy of notice in Figure 12 is that the rms values of faint stars are not improved by binning from 12 to 36 minutes. A possible reason is that the fainter a star is, the less data points are in its light curve. Most of the valid measurements are usually crowded into those days with good observing conditions. For the other days with large extinction, light curves of

faint stars are very sparse, say 1–2 points per hour, on average. When we divide these time series into equally spaced intervals with 12 or 36 minutes, many intervals are actually empty or have only one measurement. As a result, the rms of the entire light curve may be dominated by these sparse parts and will not be improved by increasing the binning time from 12 to 36 minutes. Another reason is that some systematic errors may still be buried in the photometry of stars fainter than $m_i = 14.0$. This effect raises an uncertainty in the rms at a level of several percent, which is not a serious problem for most variables stars, since the amplitudes of their brightness variations are usually larger than 10%. For transiting exoplanet searching, we abandon stars fainter than 14.0th magnitude.

5.1. Variables Found by AST3-II

5.1.1. Eclipsing Binaries

While detailed studies of the variable stars we have found are beyond the scope of this paper, we present a simple classification of the variables according to the shape and frequency analysis of their light curves. Since we have a lack of sample light curves that have a similar error model to the AST3-II observations, machine-learning methods cannot be easily employed. However, samples from this work will be used in a training library for future machine classifications. Our classification was done by two groups of people independently using the light-curve morphology, supplemented by Fourier analysis of the brightness variations in cases where the shape was not clear. Each variable was labeled only when the two groups achieved the same or similar result, after occasional robust discussion.

The first major category of variables we found are eclipsing binaries, and these can be further subdivided into Algol-type eclipsing systems (EAs), *β* Lyrae–type eclipsing systems (EBs), and W Ursae Majoris–type eclipsing variables (EWs). The EA systems have different depths between the primary and secondary minima and clearly defined times for the beginning and end of the eclipses; the most common EA systems are detached eclipsing binaries (Catelan & Smith 2015), although some of them are semidetached binaries, as, in fact, is the prototype of this class, Algol (Kolbas et al. 2015). The EB systems always show a continuous variation in brightness and have an obvious deeper primary eclipse. The EW systems also show a continuous change in brightness, but the difference between the depths of the primary and secondary minima is no longer so obvious. Sometimes this difference is indistinguishable under poor photometric precision, and the target may be easily misclassified as a pulsating star if we only consider the shape of its light curve. A frequency analysis of the light curve is needed in this situation. The EW systems consist of two components that are almost in contact; thus, most of them have periods shorter than 1 day.

In total, we have detected 117 binaries, 86 of which are new detections from the AST3-II project in 2016. There are 69 EWs, 19 EBs, and 29 EAs in our

sample. The classifications of 20 stars are not well determined, and each of them could be classified under several different variable classes, including eclipsers, pulsators, and others. For these uncertain systems, we mark them with the symbol "?" or separate different types with a pipe symbol, "|," in Table 4. We also show eight binaries with eclipse depth ≤5% that are very similar in appearance to transit signals but have a sharp "V"-shaped bottom in Figure 19.

5.1.2. Pulsating Variables

The second category of variables in our survey are the pulsating variables: δ Scuti, γ Doradus, RR Lyrae stars, Cepheids, and so on (Catelan & Smith 2015). The δ Scuti variables are late A- and early F-type stars located in the instability strip above the main-sequence belt in the Hertzsprung–Russell diagram. Their typical pulsation periods are found to be in the range from 0.02 to 0.25 days (Breger 2000). The γ Doradus stars are located in a similar position in the instability strip as the δ Scuti stars, but their pulsating periods are longer—between 0.3 and 3 days (Cuypers et al. 2009). The RR Lyrae stars are radially pulsating giant stars with spectral types from A to F with periods in the range from 0.2 to 1.0 days (Smith 2004). Cepheid variables obey a period–luminosity relation and can be divided into two subclasses—type I and type II (Catelan & Smith 2015)—based on their masses, ages, and evolutionary states. The brightness variation of most type I Cepheid variables (also known as δ Cepheids) shows a rapid rise to maximum and a slow decline back to minimum, which is similar to the variation of an RR Lyrae star but with a longer period from 1 to 60 days (Soszynski et al. 2008). Type II Cepheids generally show a relatively broad maximum and a symmetric minimum (Schmidt et al. 2004) and have periods of ~0.8–35 days and light amplitudes from 0.3 to 1.2 mag in the V band.

As for the eclipsing binary stars, our classification of pulsating variables is based on the shape of their light curves. However, since most pulsating stars have multiple frequencies, all of the variables that are classified as pulsating stars were analyzed by Fourier decomposition. The results of a frequency analysis played a very important role in deciding their nature. In our sample, there are 104 pulsators, which are classified into 29 δ Scuti stars, 35 Cepheids, and 40 RR Lyraes. Uncertain systems are labeled by "?" or "|."

6. Summary

We present some of the latest results from CHESPA. This program is based on the AST3-II telescope located at the Chinese Kunlun station at Dome A, Antarctica. This first data release contains a data set obtained in the austral winter of 2016 with target fields within the southern CVZ of *TESS*. The data set is available to the community through the website of the School of Astronomy and Space Science, Nanjing University,[28] and the Chinese Astronomical Data Center.[29] The released data consist of three parts: calibrated catalogs, light curves for general science usage, and a catalog of newfound variables. In addition, science images can be made available via

email requests to huizhang@nju.edu.cn. The science images include reduced FITS images with headers containing the observation information, including target name, world coordinate system, observation date, and exposure time.

The calibrated catalogs contain all sources found by our pipeline with an S/N above a threshold of 3σ. Observation conditions and statistics of image quality are also included in the header of each catalog (see Table 2). The light curves for general science usage include sources that are cross-matched with the sources in the APASS catalog with a limiting magnitude of $m_i \leqslant 15$. There are two subsets of light curves: (1) original light curves that inherit all the information from the corresponding catalogs and (2) polished light curves that are detrended and binned to a cadence of 12 minutes. The catalog of variables shows coordinates, magnitudes, periods, and stellar properties cross-matched with the AAVSO database and the TIC for all of the variables we have found within the southern CVZ of *TESS* (see Table 4). There are 42 variables that are matched in the variable catalog of AAVSO. Although classification is not the major goal of this work, we have achieved a high consistency with the AAVSO database. Only three of these 42 variables are not consistent: target "AST3II092.1221-71.1200" ("ACV" or "CEP"), "AST3II096.3232-71.3623" ("ROT" or "RR"), and "AST3II102.4829-71.7105" ("YSO" or "EW"). From the shape of our light curves, we think our classification is more convincing. Note that we have included the contact eclipsing binary, "EC," the detached eclipsing binary, "ED," and the semidetached eclipsing binary, "ESD," in the AAVSO database in "EW," "EA," and "EB," respectively. The two types in each pair, e.g., "EC" and "EW," are basically the same type in two different classification systems. There are 179 targets that are newly found variables, and 67 targets are also listed in the potential planet candidate list of *TESS*. Since we have only selected variables with regular shapes and obvious periods, many irregular and/or long-term variables are not included in our variable catalog. These objects will be studied and released in future works. The minimum variation reliably detected by our survey is below 5 mmag, showing that we have the ability to find transiting exoplanets. A detailed catalog of transiting exoplanet candidates found by our survey is in preparation.

This work was supported by the Natural Science Foundation of China (NSFC grants 11673011, 11333002, and 11273019) and the National Basic Research Program (973 Program) of China (grant Nos. 2013CB834900 and 2013CB834904). The authors deeply appreciate all the CHINAREs for their great effort in installing/maintaining CSTAR, CSTAR-II, AST3-I, AST3-II, and PLATO-A. This study has also been supported by the Chinese Polar Environment Comprehensive Investigation & Assessment Program (grant No. CHINARE2016-02-03), the Australian Antarctic Division, and the Australian National Collaborative Research Infrastructure Strategy administered by Astronomy Australia Limited. HZ is also grateful to the High Performance Computing Center (HPCC) of Nanjing University for reducing the data used in this paper. This research was made possible through the use of the AAVSO

Photometric All-Sky Survey (APASS), funded by the Robert Martin Ayers Sciences Fund.

Software: Sextractor (Bertin & Arnouts 1996), Swarp (Bertin et al. 2002), VARTOOLS (Hartman & Bakos 2016), Astrometry.net (Lang et al. 2010), MATLAB.

Appendix: Appendix Data

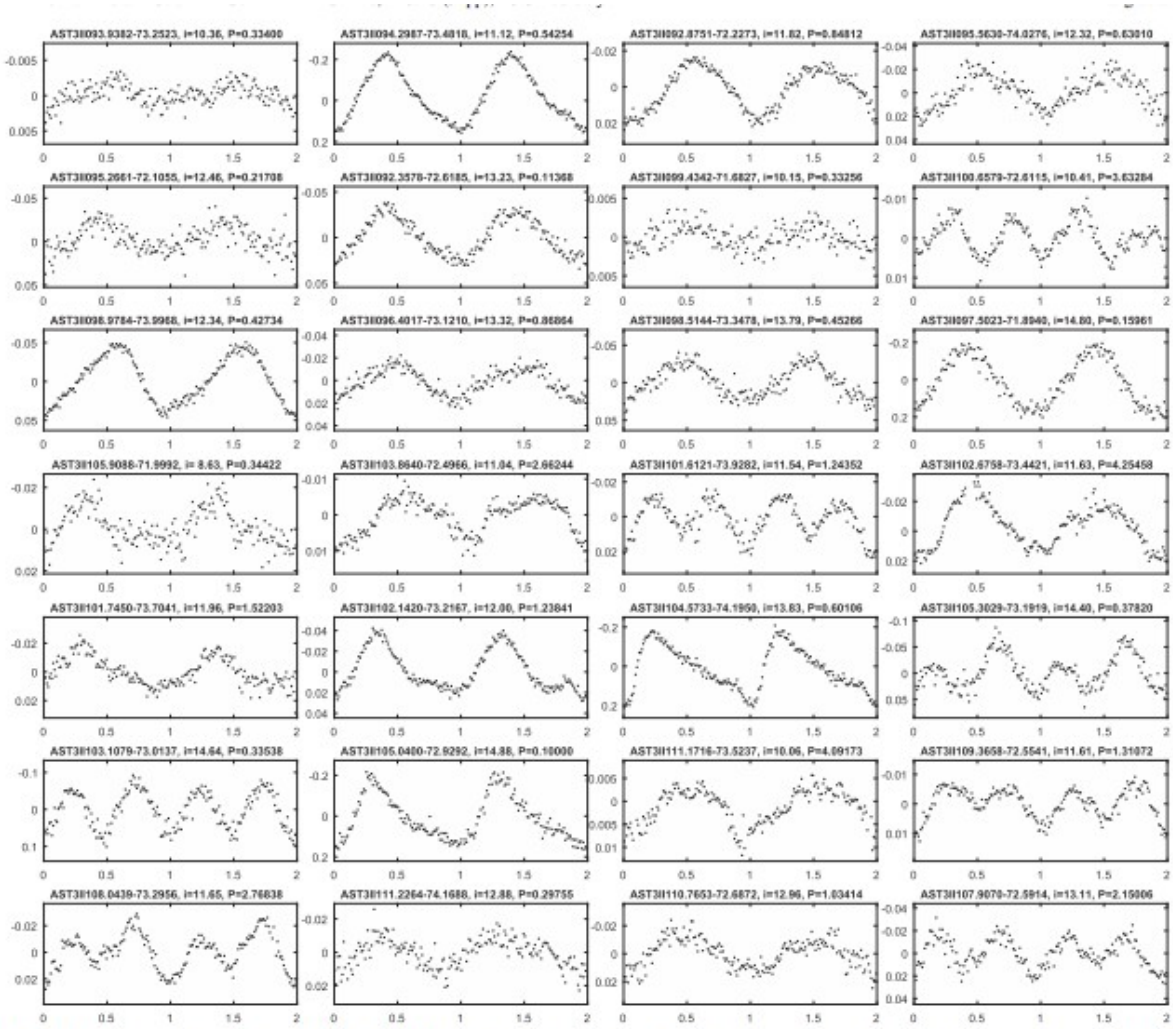

Figure 20. Pulsating variables found by AST3-II in 2016. The label above each panel contains the *i*-band median magnitude (which has been subtracted) for the curves and the period in days. The *x* and *y* axes of each panel are the phases [0, 2] (note that each light curve is folded to two times of its period, so the measurement around phase 1.5 is not identical to that around phase 0.5) and the variation in magnitude Δm_i, respectively.

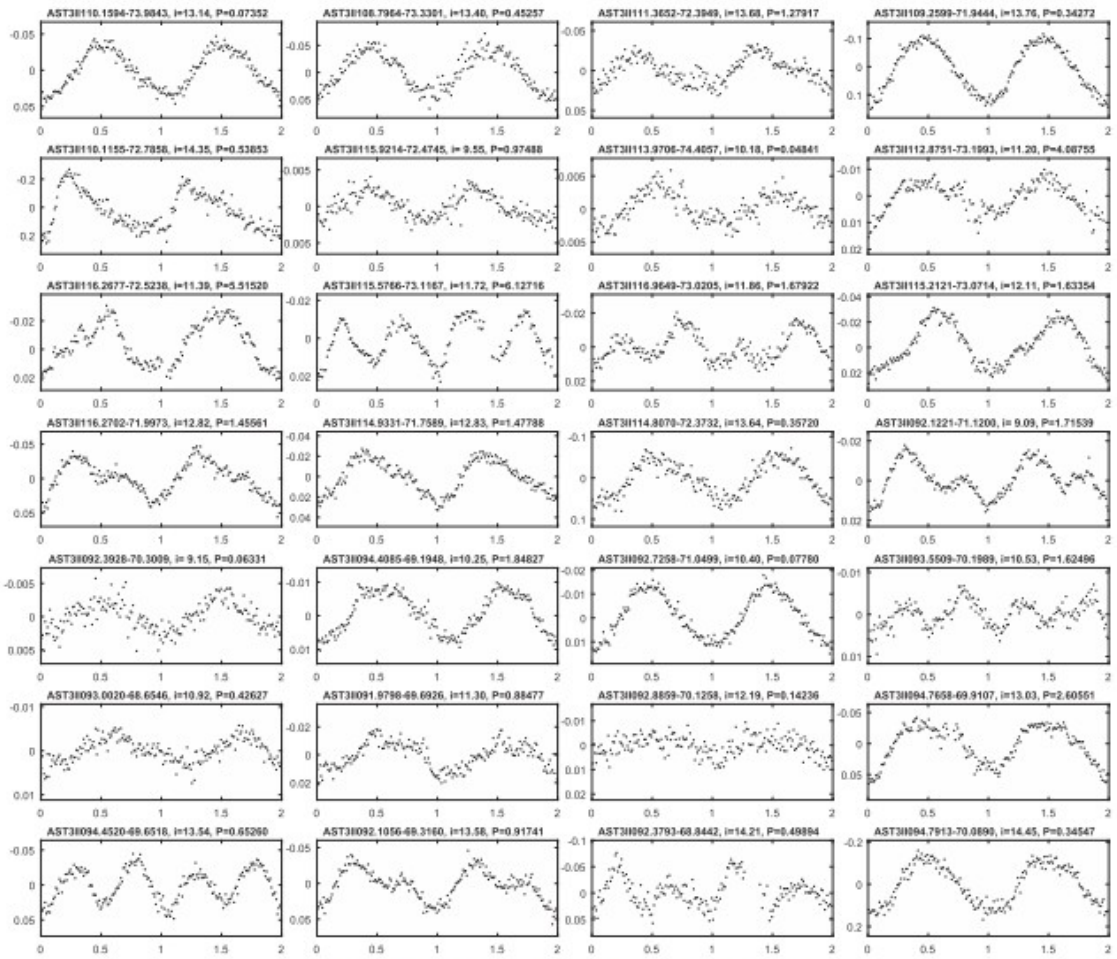

Figure 21. Pulsating variables found by AST3-II in 2016 (continued).

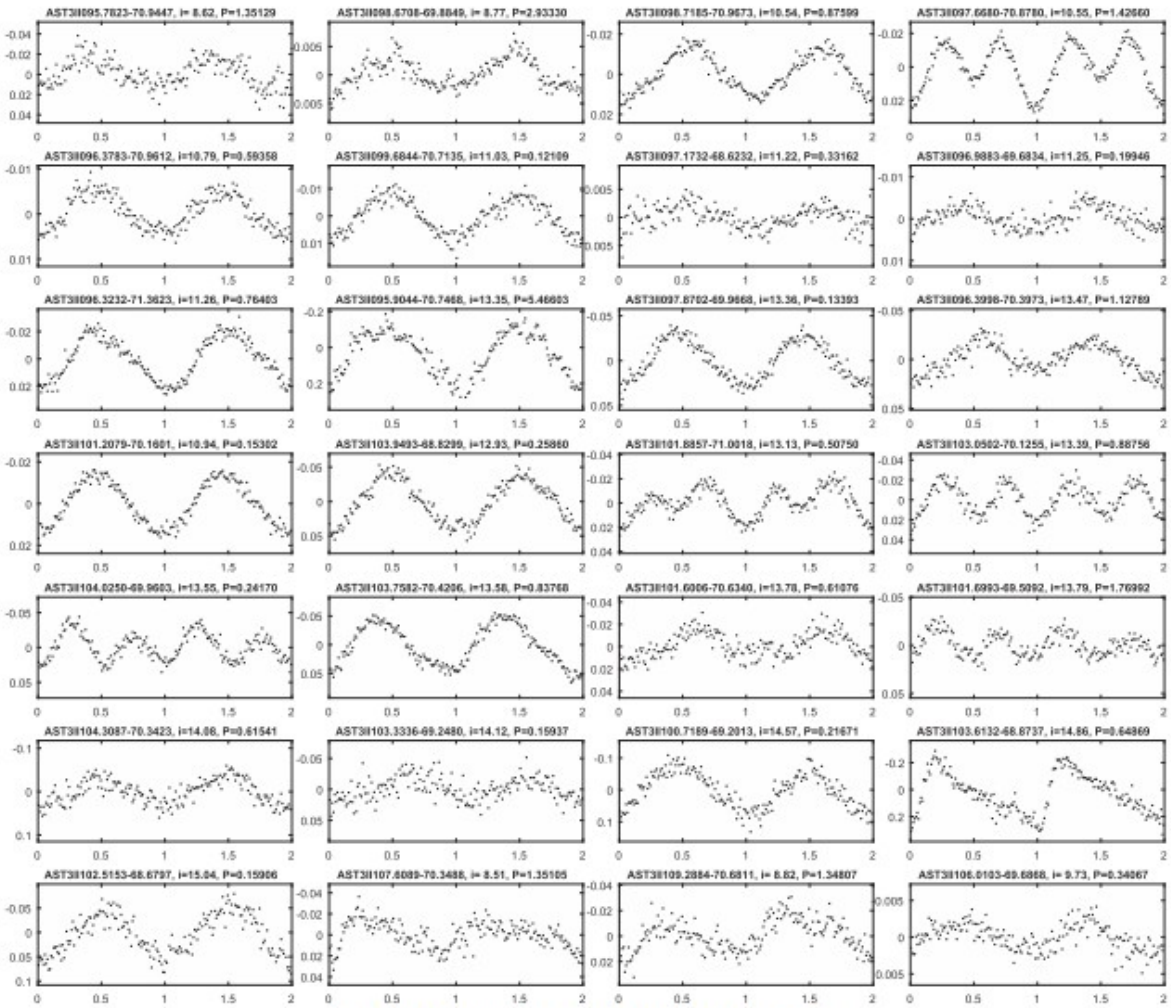

Figure 22. Pulsating variables found by AST3-II in 2016 (continued).

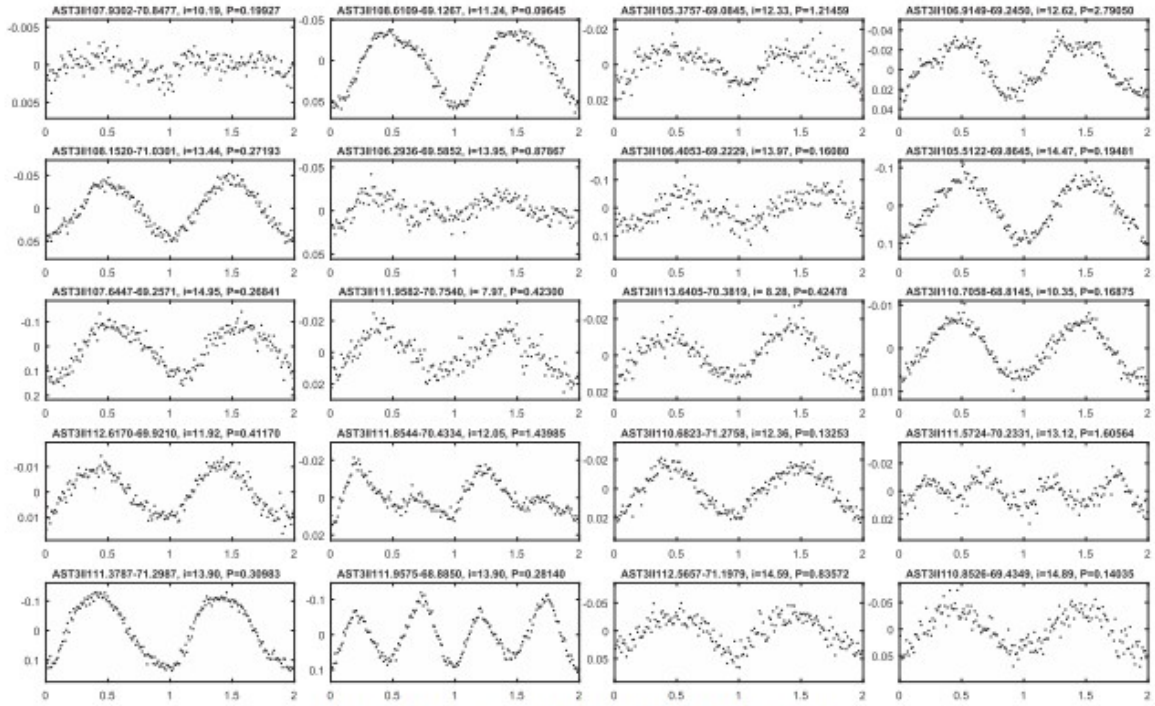

Figure 23. Pulsating variables found by AST3-II in 2016 (continued).

Table 4
Variables from AST3-II Observation in 2016

Target[a]	mag_g[b] (mag)	ID_{tic}[c]	mag_{tic}[c] (mag)	R_{tic}[c] ($R_\odot$)	M_{tic}[c] ($M_\odot$)	CTL[d] Flag	AAVSO Notation[e]	P_{aav}[e] (days)	$Type_{aav}$[e]	P_{ast3} (days)	$Type_{ast3}$[f]
AST3II111.2878-70.4038	7.57	300384180	6.63	11.0074	0.7757	0	···	···	···	0.84600	*EW*
AST3II111.9582-70.7540	7.97	300508526	7.31	16.8009	0.7123	0	···	···	···	0.42300	*RR*
AST3II102.2226-73.2995	8.14	177258735	7.53	1.5909	1.3934	1	···	···	···	4.26090	*EA*
AST3II113.6405-70.3819	8.28	453079732	7.66	2.4195	1.4143	1	···	···	···	0.42478	*RR*
AST3II111.7546-69.5154	8.45	300443831	8.25	3.0748	1.6413	1	ZZ Vol	0.84743	*EW|KE*	0.84726	*EW*
AST3II107.6089-70.3488	8.51	300039874	8.07	9.7297	0.9137	0	···	···	···	1.35105	*CEP*
AST3II095.7823-70.9447	8.62	167089430	8.05	2.8333	2.1349	1	···	···	···	1.35129	*CEP*
AST3II105.9088-71.9992	8.63	271554516	8.43	2.0157	1.6519	1	···	···	···	0.34422	*RR*
AST3II098.6708-69.8849	8.77	167344043	8.50	1.2255	0.9718	1	···	···	···	2.93330	*CEP*
AST3II109.2884-70.6811	8.82	300160946	8.29	0.4974	0.4977	0	···	···	···	1.34807	*CEP*
AST3II092.1221-71.1200	9.09	41259805	8.85	1.7874	1.9437	1	ASAS J060829-7107.2	1.71443	*ACV*	1.71539	*CEP*
AST3II092.3928-70.3009	9.15	41360272	8.83	5.8939	1.7469	0	···	···	···	0.06331	*DSCT*
AST3II115.9214-72.4745	9.55	272127517	9.33	1.8948	1.4190	1	···	···	···	0.97488	*RR*
AST3II106.0103-69.6868	9.73	299899924	9.40	1.8372	1.6901	1	···	···	···	0.34067	*RR*
AST3II091.3523-69.0324	10.00	41172665	9.76	2.9070	1.4465	1	···	···	···	1.73012	*EA*
AST3II111.1716-73.5237	10.06	271795905	9.76	1.2572	1.2002	1	···	···	···	4.09173	*CEP*
AST3II099.4342-71.6827	10.15	167416361	9.86	1.3734	1.2409	1	···	···	···	0.33256	*DSCT*
AST3II113.9706-74.4057	10.18	271971704	9.88	2.4153	1.6948	1	···	···	···	0.04841	*DSCT*
AST3II107.9302-70.8477	10.19	300086363	9.90	3.4197	1.1236	1	···	···	···	0.19927	*RR|DSCT*
AST3II094.4085-69.1948	10.25	41595212	9.98	1.6549	1.2327	1	···	···	···	1.84827	*CEP*
AST3II110.7058-68.8145	10.35	300327061	10.00	1.8652	1.4767	1	···	···	···	0.16875	*RR*
AST3II093.9382-73.2523	10.36	141868094	10.08	2.0054	1.4850	1	···	···	···	0.33400	*DSCT ?*
AST3II092.7258-71.0499	10.40	41362881	10.12	3.3323	1.5383	1	···	···	···	0.07780	*DSCT*
AST3II100.6579-72.6115	10.41	176872638	10.26	···	···	0	···	···	···	3.63284	*CEP*
AST3II093.5509-70.1989	10.53	41483281	10.24	1.3562	1.5535	1	···	···	···	1.62496	*CEP?*
AST3II098.7185-70.9673	10.54	167361929	10.23	2.0106	1.4631	1	···	···	···	0.87599	*RR*
AST3II097.6680-70.8780	10.55	167249549	10.22	3.4671	1.4169	1	···	···	···	1.42660	*CEP*
AST3II097.5428-69.3784	10.77	167248486	10.45	1.8288	1.4376	1	···	···	···	0.80528	*EW*
AST3II096.3783-70.9612	10.79	167163582	10.49	···	···	0	···	···	···	0.59358	*RR*
AST3II094.1155-74.4470	10.89	141871560	10.51	1.9905	1.5946	1	NSV 2922	0.63045	*EW*	0.63052	*EW*
AST3II093.0020-68.6546	10.92	41463672	10.68	1.8286	1.5935	1	···	···	···	0.42627	*RR*
AST3II101.2079-70.1601	10.94	176960346	10.66	1.5066	1.3332	1	···	···	···	0.15302	*DSCT*
AST3II093.7797-71.5701	10.96	41533230	10.66	1.3007	1.1688	1	ASAS J061507-7134.2	1.42051	*EC|DCEP − FO|ESD*	1.42086	*EW*
AST3II099.6844-70.7135	11.03	167417105	10.70	2.6568	1.7240	1	···	···	···	0.12109	*DSCT*
AST3II103.8640-72.4966	11.04	177349463	10.76	1.0578	1.0657	1	···	···	···	2.66244	*CEP*
AST3II094.2987-73.4818	11.12	141870888	10.79	···	···	0	RV Men	0.54229	*RRC*	0.54254	*RR*
AST3II091.6806-72.2152	11.17	141766191	10.83	1.4415	1.0253	1	···	···	···	0.37354	*EW*
AST3II112.8751-73.1993	11.20	271891181	10.85	1.0634	0.9906	1	···	···	···	4.08755	*CEP*
AST3II097.1732-68.6232	11.22	167207431	10.90	1.7974	1.2539	1	···	···	···	0.33162	*RR*
AST3II110.2915-71.8165	11.24	300291165	11.13	···	···	0	ASAS J072110-7149.0	0.35427	*EA*	0.35434	*EB|EW*
AST3II108.6109-69.1267	11.24	300139147	10.91	1.7439	1.5913	1	ASAS J071427-6907.6	0.09647	*DSCT*	0.09645	*DSCT*
AST3II096.9883-69.6834	11.25	167203167	10.94	1.3137	1.1658	1	···	···	···	0.19946	*DSCT*
AST3II096.3232-71.3623	11.26	167163906	10.91	0.6935	0.8363	1	ASAS J062517-7121.9	0.75890	*ROT*	0.76403	*RR*
AST3II113.5745-74.2172	11.30	271904441	11.68	1.3449	1.2080	1	···	···	···	0.69178	*EW ?*
AST3II091.9798-69.6926	11.30	41256640	10.99	1.6020	1.4501	1	···	···	···	0.88477	*RR*
AST3II115.5460-72.9271	11.31	272087157	10.91	···	···	0	···	···	···	0.31996	*EW?*
AST3II112.8364-69.8340	11.38	300559128	10.99	1.3798	1.2397	1	···	···	···	4.17330	*EA*

Table 4
(Continued)

Target[a]	mag$_j$[b] (mag)	ID$_{tic}$[c]	mag$_{tic}$[c] (mag)	R_{tic}[c] ($R_\odot$)	M_{tic}[c] ($M_\odot$)	CTL[d] Flag	AAVSO Notation[e]	P_{aas}[e] (days)	Type$_{aas}$[e] ···	P_{ast3} (days)	Type$_{ast3}$[f]
AST3II102.2495-73.3640	11.39	177258700	10.95	2.3260	1.5876	1	ASAS J064900-7321.8	0.68796	*EC*	0.68792	*EW*
AST3II116.2677-72.5238	11.39	272128498	10.98	···	···	0	···	···	···	5.51520	*CEP*
AST3II107.5256-69.5379	11.47	300034498	11.19	1.4353	1.2911	1	ASAS J071006-6932.3	1.78290	*ED*	1.78150	*EA*
AST3II101.6121-73.9282	11.54	177254093	11.17	2.0275	1.4758	1	···	···	···	1.24352	*CEP*
AST3II109.3658-72.5541	11.61	271640842	11.34	1.3425	1.1772	1	···	···	···	1.31072	*CEP*
AST3II102.6758-73.4421	11.63	177283525	11.33	1.3975	1.0873	1	···	···	···	4.25458	*CEP*
AST3II108.0439-73.2956	11.65	391946675	11.27	···	···	0	···	···	···	2.76838	*CEP*
AST3II115.5766-73.1167	11.72	272087305	11.38	1.3772	1.1055	1	···	···	···	6.12716	*CEP*
AST3II096.9914-70.5949	11.75	167203947	11.48	···	···	0	ASAS J062758-7035.7	0.62027	*EC|RRC| ESD*	0.62036	*EW*
AST3II094.9034-72.0335	11.79	141914317	11.48	1.2774	1.0286	1	ASAS J061937-7202.0	0.43718	*EC*	0.43722	*EW*
AST3II092.8751-72.2273	11.82	141807839	11.19	···	···	0	···	···	···	0.84812	*RR*
AST3II116.9649-73.0205	11.86	272190346	11.57	2.1749	2.1012	1	···	···	···	1.67922	*CEP*
AST3II108.2432-69.0400	11.90	300091984	11.57	1.3587	1.2205	1	···	···	···	2.16220	*EA*
AST3II112.6170-69.9210	11.92	300556532	11.54	···	···	0	···	···	···	0.41170	*RR*
AST3II098.2398-68.9722	11.93	167307524	11.86	1.2569	1.1312	1	···	···	···	0.60335	*EA*
AST3II101.7450-73.7041	11.96	177253966	11.60	2.4601	1.5650	1	···	···	···	1.52203	*CEP*
AST3II108.0795-74.3732	12.00	391947238	11.67	1.2661	1.1390	1	···	···	···	5.66890	*EA*
AST3II102.1420-73.2167	12.00	177258779	11.64	···	···	0	···	···	···	1.23841	*CEP*
AST3II105.4951-72.9830	12.01	388180826	11.86	1.5144	1.3659	1	···	···	···	0.37226	*EW*
AST3II101.8520-71.5969	12.03	177017182	11.73	2.0432	1.2507	1	···	···	···	0.32736	*EW*
AST3II091.1306-72.1367	12.03	141713380	11.72	1.0337	0.9785	1	···	···	···	0.38590	*EW|RR*
AST3II111.8544-70.4334	12.05	300449915	11.68	1.0956	1.0564	1	···	···	···	1.43985	*CEP*
AST3II102.4683-73.4007	12.07	177283493	11.77	···	···	0	···	···	···	0.75318	*EB*
AST3II091.3416-69.7834	12.10	41173515	11.77	1.6011	1.4493	1	ASAS J060521-6947.1	0.59305	*EC|RRC*	0.59284	*EW|RR*
AST3II115.2121-73.0714	12.11	272085493	11.76	···	···	0	···	···	···	1.63354	*CEP*
AST3II092.8859-70.1258	12.19	41363877	11.83	1.1597	1.0548	1	···	···	···	0.14236	*DSCT|EA*
AST3II114.8573-73.7690	12.20	271999940	11.88	1.1989	1.0777	1	ASAS J073926-7346.2	0.56424	*ESD|EC*	0.56410	*EB*
AST3II098.6131-68.9374	12.27	167339240	11.95	1.1524	1.0495	1	···	···	···	2.18525	*EA*
AST3II098.6280-72.0523	12.30	142105466	11.95	1.1155	1.0522	1	ASAS J063431-7203.1	0.43320	*EC|ESD*	0.43318	*EW*
AST3II102.0928-69.5721	12.32	177018607	12.00	1.0583	0.9855	0	···	···	···	0.36118	*EW*
AST3II095.5630-74.0276	12.32	141944605	11.99	1.2912	1.1605	1	···	···	···	0.63010	*DSCT* ?
AST3II105.3757-69.0845	12.33	177238312	12.02	1.3690	1.2298	0	···	···	···	1.21459	*CEP*
AST3II098.9784-73.9968	12.34	142106818	11.94	···	···	0	···	···	···	0.42734	*RR*
AST3II096.5406-72.2855	12.36	142013932	12.02	1.2720	1.1440	0	···	···	···	5.50270	*EA*
AST3II110.6823-71.2758	12.36	300328626	12.08	1.5047	1.3567	0	···	···	···	0.13253	*DSCT*
AST3II092.9887-69.2780	12.43	41464424	12.05	0.9920	0.9401	1	ASAS J061157-6916.7	0.33890	*ESD|DSCT| EC*	0.33890	*EW*
AST3II108.2786-71.7907	12.44	300137432	12.31	0.9607	0.9175	1	TY Vol	0.32763	*EW*	0.32762	*EW*
AST3II095.2661-72.1055	12.46	141914372	12.10	···	···	0	···	···	···	0.21708	*RR*
AST3II094.9934-69.9677	12.48	167005326	12.16	1.4051	1.2629	0	···	···	···	0.72018	*EB*
AST3II107.4982-72.1355	12.50	391927558	12.21	1.3305	1.1161	0	ASAS J070959-7208.2	0.54292	*ESD|EC*	0.54316	*EB*
AST3II102.4826-70.3848	12.50	177032797	12.35	1.2760	0.9323	1	···	···	···	0.28482	*EW*
AST3II096.2029-72.0109	12.52	142013583	12.22	1.1731	1.0646	0	···	···	···	0.32200	*EW*?
AST3II105.9193-70.7796	12.58	299900499	12.29	1.0019	0.9471	1	ASAS J070341-7046.8	0.37554	*EC|DSCT*	0.37562	*EW*
AST3II094.4370-73.0193	12.59	141870501	12.33	1.2483	1.1240	0	ASAS J061745-7301.2	0.53189	*ESD*	0.53202	*EB*
AST3II106.8398-69.6943	12.59	300009837	12.42	1.4030	1.2610	0	ASAS J070722-6941.7	0.36651	*EC*	0.36652	*EW*
AST3II106.9149-69.2450	12.62	300010099	12.19	···	···	0	···	···	···	2.79050	*CEP*

Table 4
(Continued)

Target[a]	mag$_i$[b] (mag)	ID$_{tic}$[c]	mag$_{tic}$[c] (mag)	R_{tic}[c] ($R_\odot$)	M_{tic}[c] ($M_\odot$)	CTL[d] Flag	AAVSO Notation[e]	P_{aas}[e] (days)	Type$_{aas}$[e] ···	P_{ast3} (days)	Type$_{ast3}$[f]
AST3II103.5842-70.8694	12.65	177113550	12.32	1.2062	1.0899	0	···	···	···	0.34158	*EW*
AST3II102.4829-71.7105	12.70	177033514	12.44	1.5974	1.4456	0	ASASSN-V J064955.83-714237.5	···	*YSO*	1.00686	*EW*
AST3II113.0724-72.9353	12.72	271892852	12.33	···	···	0	···	···	···	4.14840	*EA|RS*
AST3II093.7557-72.2885	12.73	141869057	12.38	1.0858	1.0038	0	···	···	···	0.43568	*EW*
AST3II108.4769-72.3906	12.74	271594955	12.33	1.2730	1.1448	0	ASAS J071355-7223.5	0.41165	*EC*	0.41164	*EW*
AST3II116.9547-73.9117	12.77	272191334	12.35	1.4148	1.2720	0	ASAS J074749-7354.7	0.41929	*EC*	0.41930	*EW*
AST3II116.2702-71.9973	12.82	272128027	12.47	···	···	0	···	···	···	1.45561	*CEP*
AST3II107.6780-73.6250	12.83	391926737	12.45	1.4546	1.3092	0	ASAS J071043-7337.5	0.59408	*ESD|EC*	0.59408	*EB*
AST3II108.2001-71.3165	12.83	300137123	12.55	1.2374	1.1150	0	···	···	···	2.28680	*EA*
AST3II114.9331-71.7589	12.83	300709487	12.43	···	···	0	···	···	···	1.47788	*CEP*
AST3II097.6441-71.6785	12.86	167250056	12.50	1.1120	1.0214	0	···	···	···	0.85770	*EB*
AST3II092.9678-71.2428	12.87	41362672	12.50	···	···	0	···	···	···	0.99728	*EA*
AST3II111.2264-74.1688	12.88	271795440	12.54	0.8139	0.7894	1	···	···	···	0.29755	*DSCT|RR*
AST3II106.3396-69.1610	12.90	299939799	12.60	1.3331	1.1974	0	YZ Vol	1.57097	*EA*	0.78532	*EB*
AST3II098.3455-70.1247	12.92	167338355	12.45	1.3545	0.8715	0	ASAS J063323-7007.5	0.28836	*EC*	0.28836	*EW*
AST3II103.9493-68.8299	12.93	177116027	12.60	1.3316	1.1961	0	···	···	···	0.25860	*RR*
AST3II110.7653-72.6872	12.96	271724440	12.65	···	···	0	···	···	···	1.03414	*CEP*
AST3II094.7658-69.9107	13.03	167005378	12.62	···	···	0	···	···	···	2.60551	*CEP*
AST3II107.9070-72.5914	13.11	391946253	12.81	1.3958	1.2544	0	···	···	···	2.15006	*CEP*
AST3II111.5724-70.2331	13.12	300443364	12.74	1.5702	1.4194	0	···	···	···	1.60564	*CEP*
AST3II101.8857-71.0018	13.13	177016884	12.76	···	···	0	···	···	···	0.50750	*RR*
AST3II110.1594-73.9843	13.14	271697152	12.68	1.5338	1.3845	0	···	···	···	0.07352	*DSCT*
AST3II096.4438-71.4297	13.18	167163979	12.82	1.6282	1.4757	0	···	···	···	0.41730	*EW*
AST3II106.6609-71.2478	13.22	299945169	13.00	0.8687	0.8427	1	···	···	···	0.38934	*EW*
AST3II092.3578-72.6185	13.23	141806774	12.91	1.7082	1.5550	0	···	···	···	0.11368	*DSCT*
AST3II090.6260-73.7799	13.28	141711100	12.95	1.1278	1.0322	0	ASAS J060230-7346.8	0.43001	*EC|RRC| DSCT|ESD*	0.42996	*EW*
AST3II104.7510-73.5358	13.31	177387467	12.92	1.4841	1.3371	0	···	···	···	0.78224	*EW*
AST3II113.2799-73.8991	13.31	271893557	12.96	0.9121	0.8799	1	···	···	···	0.29744	*EW*
AST3II096.3806-73.2253	13.32	141979627	12.90	0.8276	0.8034	1	···	···	···	0.24426	*EW*
AST3II096.4017-73.1210	13.32	141979700	12.95	···	···	0	···	···	···	0.86864	*RR*
AST3II100.2953-72.5818	13.34	142149364	12.90	···	···	0	···	···	···	4.33840	*EA*
AST3II105.7928-73.9199	13.35	388181338	12.99	1.7702	1.6185	0	···	···	···	1.58656	*EB*
AST3II095.9044-70.7468	13.35	167089250	12.90	···	···	0	ASASSN-V J062337.04-704448.5	5.52500	*CWB*	5.46603	*CWB*
AST3II097.8702-69.9668	13.36	167251575	13.01	1.7199	1.5667	0	···	···	···	0.13393	*DSCT*
AST3II114.7338-72.9593	13.37	271999317	12.89	1.2502	1.1256	0	···	···	···	0.32968	*EW*
AST3II096.1773-72.9143	13.38	141979847	12.97	1.1861	1.0743	0	···	···	···	0.35684	*EW*
AST3II103.0502-70.1255	13.39	177075511	13.11	···	···	0	···	···	···	0.88756	*RR*
AST3II095.9351-70.8911	13.40	167089377	13.12	···	···	0	···	···	···	0.20546	*EW*
AST3II108.7964-73.3301	13.40	271639568	13.03	1.2686	1.1411	0	···	···	···	0.45257	*RR*
AST3II111.1322-70.1645	13.42	300330083	13.00	···	···	0	···	···	···	1.13160	*EA*
AST3II107.1686-70.9064	13.44	300015474	13.14	···	···	0	···	···	···	0.33012	*EW*
AST3II108.1520-71.0301	13.44	300086267	13.10	1.7057	1.5524	0	···	···	···	0.27193	*DSCT*
AST3II096.3998-70.3973	13.47	167163087	13.13	1.3377	1.2015	0	···	···	···	1.12789	*CEP*
AST3II104.8638-74.1627	13.50	177387851	13.17	···	···	0	···	···	···	2.50724	*EA*
AST3II094.4520-69.6518	13.54	41595694	13.17	1.5192	1.3705	0	···	···	···	0.65260	*RR*
AST3II104.0250-69.9603	13.55	177161450	13.18	···	···	0	···	···	···	0.24170	*DSCT*
AST3II102.1568-69.3738	13.55	177018730	13.25	0.9939	0.9415	0	···	···	···	1.36585	*EA?*

Table 4
(Continued)

Target[a]	mag$_j$[b] (mag)	ID$_{tic}$[c]	mag$_{tic}$[c] (mag)	R_{tic}[c] ($R_\odot$)	M_{tic}[c] ($M_\odot$)	CTL[d] Flag	AAVSO Notation[e]	P_{aas}[e] (days)	Type$_{aas}$[e] ···	P_{ast3} (days)	Type$_{ast3}$[f]
AST3II092.5544-73.8344	13.57	141809397	13.19	1.1713	1.0632	0	···	···	···	0.33874	*EW*
AST3II092.1056-69.3160	13.58	41331305	13.15	0.6797	0.6541	0	···	···	···	0.91741	*RR*
AST3II103.7582-70.4206	13.58	177115026	13.30	···	···	0	···	···	···	0.83768	*RR*
AST3II100.0861-72.5257	13.59	142149387	13.26	1.1969	1.0826	0	ASASSN-VJ064020.58-723133.0	0.49752	*EW*	0.49736	*EW*
AST3II091.6046-69.4909	13.60	41227678	13.12	0.9864	0.9361	0	ASAS J060625-6929.4	0.37134	*EC|ESD*	0.37132	*EW*
AST3II095.3040-72.3847	13.64	141945928	13.30	1.2085	1.0916	0	ASASSN-V J062112.94-722305.3	0.43400	*EW*	0.43378	*EW*
AST3II114.8070-72.3732	13.64	271998864	13.26	1.6298	1.4772	0	···	···	···	0.35720	*RR*
AST3II095.8987-69.5264	13.67	167088180	13.38	···	···	0	···	···	···	1.95352	*EA*
AST3II111.3652-72.3949	13.68	271797324	13.28	···	···	0	···	···	···	1.27917	*CEP*
AST3II116.4310-73.9974	13.69	···	···	···	···	0	···	···	···	0.50372	*EW*
AST3II098.3039-71.3062	13.73	167309182	13.41	1.0812	1.0008	0	···	···	···	1.33115	*EA*
AST3II109.2599-71.9444	13.76	300160216	13.46	1.6193	1.4670	0	ASASSN-V J071702.37-715640.0	0.34266	*RRC*	0.34272	*RR*
AST3II107.5824-68.7888	13.78	300035002	13.54	···	···	0	···	···	···	1.33990	*EA*
AST3II101.6006-70.6340	13.78	176980970	13.25	···	···	0	···	···	···	0.61076	*RR*
AST3II109.1080-68.9219	13.79	300162041	13.55	···	···	0	···	···	···	0.46402	*EA*
AST3II098.5144-73.3478	13.79	142104577	13.46	···	···	0	···	···	···	0.45266	*RR*
AST3II101.6993-69.5092	13.79	176986279	13.43	···	···	0	···	···	···	1.76992	*CEP*
AST3II104.5733-74.1950	13.83	177355123	13.47	1.3275	1.1924	0	ASAS J065818-7411.7	0.60111	*RRAB*	0.60106	*RR*
AST3II096.5462-68.5901	13.86	167125813	13.46	1.2416	1.1185	0	ASAS J062611-6835.4	0.27978	*ESD|EC*	0.38862	*EW*
AST3II111.3787-71.2987	13.90	300384759	13.60	1.3078	1.1750	0	ASASSN-V J072530.96-711755.7	0.30986	*RRC*	0.30983	*RR*
AST3II111.9575-68.8850	13.90	300448831	13.56	···	···	0	···	···	···	0.28140	*DSCT*
AST3II106.2936-69.5852	13.95	299939522	13.46	···	···	0	···	···	···	0.87867	*RR*
AST3II104.9029-73.9904	13.96	177387750	13.69	1.0375	0.9716	0	···	···	···	0.40066	*EW*
AST3II097.2789-73.7791	13.97	142050170	13.58	0.9329	0.8965	0	···	···	···	0.28862	*EW*
AST3II106.4053-69.2229	13.97	299943998	13.60	···	···	0	···	···	···	0.16080	*DSCT*
AST3II109.7742-72.5553	14.00	271695366	13.69	1.3067	1.1741	0	···	···	···	2.62150	*EA*
AST3II099.4564-73.5644	14.02	142142482	13.77	1.2053	1.0892	0	···	···	···	0.37834	*EW*
AST3II098.1909-70.8216	14.03	167308872	13.66	1.1810	1.0704	0	···	···	···	1.19986	*EA*
AST3II091.9501-69.7476	14.04	41256694	13.74	1.1345	1.0369	0	···	···	···	0.39314	*EW*
AST3II093.4959-69.4043	14.07	41484182	13.62	1.4363	1.2920	0	···	···	···	0.56982	*EW*
AST3II117.2315-72.1701	14.08	272189663	13.65	1.0356	0.9703	0	···	···	···	0.25154	*EW*
AST3II107.0916-70.4105	14.08	300015200	13.77	···	···	0	···	···	···	0.60962	*EB*
AST3II113.0538-69.9661	14.08	300600720	13.65	1.3886	1.2477	0	···	···	···	1.15242	*EB|EA*
AST3II104.3087-70.3423	14.08	177163611	13.67	···	···	0	···	···	···	0.61541	*RR*
AST3II113.2682-72.2934	14.09	271892411	13.78	1.2579	1.1320	0	···	···	···	1.11378	*EA|EB*
AST3II113.8272-74.2497	14.09	271971611	13.94	1.2426	1.1193	0	···	···	···	0.34376	*EW*
AST3II094.2495-68.7334	14.09	41594692	13.80	1.4040	1.2620	0	···	···	···	1.96580	*EA*
AST3II103.9694-71.9303	14.10	177114179	13.87	···	···	0	···	···	···	0.23812	*EW*
AST3II105.7290-69.7021	14.10	284196017	13.73	···	···	0	···	···	···	0.26174	*EW*
AST3II103.3336-69.2480	14.12	177078161	13.79	···	···	0	···	···	···	0.15937	*DSCT*
AST3II092.0825-72.1979	14.16	141766811	13.74	···	···	0	···	···	···	3.24340	*EA*
AST3II092.3793-68.8442	14.21	41339662	13.90	1.1181	1.0256	0	···	···	···	0.49894	*RR|DSCT*
AST3II094.8862-73.8941	14.22	141940658	13.90	1.2313	1.1100	0	···	···	···	0.40800	*EW*
AST3II102.0101-69.6037	14.24	177018590	13.78	1.0681	0.9921	0	ASASSN-V J064802.44-693613.4	0.31616	*EW*	0.31616	*EW*
AST3II096.6214-74.2658	14.30	142015305	13.92	···	···	0	···	···	···	1.15166	*EA*
AST3II104.8267-73.9244	14.33	177387712	14.17	···	···	0	···	···	···	0.38164	*EB*
AST3II106.4445-68.6182	14.35	299943609	14.14	1.4526	1.3073	0	···	···	···	1.09910	*EB*

Table 4
(Continued)

Target[a]	$mag_{i,b}$ (mag)	ID_{tic}[c]	mag_{tic}[c] (mag)	R_{tic}[c] ($R_\odot$)	M_{tic}[c] ($M_\odot$)	CTL[d] Flag	AAVSO Notation[e]	P_{aas}[e] (days)	$Type_{aas}$[e]	P_{ast3} (days)	$Type_{ast3}$[f]
AST3II110.1155-72.7858	14.35	271696340	14.24	1.2130	1.0952	0	ASASSN-V J072027.77-724709.6	0.53787	*RRAB*	0.53853	*RR*
AST3II110.5742-71.7080	14.39	300328886	13.99	1.1655	1.0590	0	···	···	···	0.45036	*EW*
AST3II107.2662-69.2645	14.40	300014528	14.00	1.2244	1.1043	0	···	···	···	1.23152	*EB*
AST3II105.3029-73.1919	14.40	370236528	14.11	···	···	0	···	···	···	0.37820	*DSCT*
AST3II103.8244-72.1353	14.41	177349687	14.35	1.0011	0.9465	0	···	···	···	0.33874	*EW*
AST3II111.5857-69.3929	14.42	300443903	13.89	···	···	0	···	···	···	0.76492	*EA*
AST3II112.6964-71.0418	14.42	300558347	14.10	1.4076	1.2653	0	···	···	···	0.40474	*EB|EW*
AST3II094.7913-70.0890	14.45	167005196	14.10	···	···	0	···	···	···	0.34547	*RR*
AST3II102.8140-69.3139	14.47	177035211	14.14	1.2512	1.1264	0	···	···	···	0.38158	*EB*
AST3II105.5122-69.8645	14.47	284196104	14.20	1.6581	1.5050	0	···	···	···	0.19481	*DSCT*
AST3II114.2903-71.7404	14.49	300655606	14.16	1.4035	1.2615	0	···	···	···	0.37428	*EW*
AST3II097.2290-69.1479	14.55	167206981	14.29	1.1424	1.0424	0	···	···	···	0.40836	*EW*
AST3II100.7189-69.2013	14.57	176936445	14.24	0.8807	0.8534	0	···	···	···	0.21671	*DSCT*
AST3II112.5657-71.1979	14.59	300557359	14.11	···	···	0	···	···	···	0.83572	*RR*
AST3II103.9372-73.1591	14.61	177350624	14.22	0.7959	0.7707	0	SSS-J065544.7-730933	0.29535	*EW*	0.29536	*EW*
AST3II116.7978-74.0328	14.62	272187821	14.26	···	···	0	SSS-J074711.5-740158	0.38556	*EW*	0.38544	*EW*
AST3II105.7603-70.1559	14.64	284196250	14.47	···	···	0	···	···	···	0.46078	*EB|EA*
AST3II107.1584-69.0159	14.64	300014365	14.28	1.1028	1.0152	0	···	···	···	0.38024	*EW*
AST3II103.1079-73.0137	14.64	177306954	14.37	1.0519	0.9813	0	···	···	···	0.33538	*DSCT|EW*
AST3II111.1086-69.0101	14.68	300378377	14.30	1.1978	1.0833	0	···	···	···	0.39342	*EW*
AST3II096.3027-73.3588	14.70	141979538	14.42	···	···	0	···	···	···	0.37346	*EB|EW*
AST3II108.9435-69.6865	14.70	300158892	14.35	1.5320	1.3827	0	···	···	···	0.64514	*EW*
AST3II117.0482-72.9081	14.71	272190253	14.36	1.1212	1.0277	0	···	···	···	0.28176	*EW*
AST3II108.7658-72.9983	14.72	271639765	14.44	1.1647	1.0584	0	···	···	···	2.27788	*EA*
AST3II111.1314-74.2812	14.76	271795366	14.43	1.0413	0.9741	0	···	···	···	0.35092	*EW*
AST3II114.7555-72.2977	14.79	271998796	14.65	···	···	0	···	···	···	0.26528	*EW*
AST3II098.0495-69.9626	14.79	167308253	14.38	1.4496	1.3044	0	···	···	···	0.57484	*EW*
AST3II108.1248-70.2486	14.79	300086700	14.51	1.6266	1.4741	0	···	···	···	0.88768	*EA|EB*
AST3II097.5023-71.8940	14.80	167250176	14.59	···	···	0	···	···	···	0.15961	*DSCT*
AST3II103.6132-68.8737	14.86	177112378	14.47	···	···	0	ASASSN-V J065427.19-685225.2	0.64953	*RRAB*	0.64869	*RR*
AST3II105.0400-72.9292	14.88	177387115	14.39	1.3128	1.1794	0	ASASSN-V J070009.61-725545.1	0.09995	*HADS*	0.10000	*DSCT*
AST3II110.8526-69.4349	14.89	300327486	14.46	···	···	0	···	···	···	0.14035	*DSCT*
AST3II107.6447-69.2571	14.95	300039207	14.58	1.7947	1.6443	0	···	···	···	0.26841	*RR*
AST3II102.5153-68.6797	15.04	177022890	14.65	···	···	0	···	···	···	0.15906	*DSCT*

Notes.
[a] IDs of AST3-II targets in the format "AST3II+R.A.+decl."
[b] The *i*-band magnitudes from the APASS catalog.
[c] IDs, *TESS* magnitudes, stellar radii, and stellar masses from the TIC (Stassun et al. 2018).
[d] CTL flags; 1 means that this target is also selected in the CTL of *TESS* (Stassun et al. 2018).
[e] Names, periods, and type designations from the AAVSO database. The explanation for each type designation is in footnote f.
[f] Variable-star type designations following VSX. *ACV*: α^2 Canum Venaticorum variables. *CEP*: Cepheids. *CWB*: W Virginis variables with periods shorter than 8 days; also known as BL Herculis variables. *DSCT*: variables of the δ Scuti type (those with amplitudes larger than 0.15 mag and asymmetric light curves are designated *HADS*). *EA* (*ED*): Algol eclipsing systems. *EB* (*ESD*): β Lyrae–type eclipsing systems. *EW* (*EC*): W Ursae Majoris–type eclipsing variables. *ROT*: spotted stars that were not classified into a particular class. *RR* (*RRAB*/*RRC*): variables of the RR Lyrae type. *RS*: RS Canum Venaticorum–type binary systems. *YSO*: young stellar object of unspecified variable type; https://www.aavso.org/vsx/index.php?view=about.vartypes.
(This table is available in machine-readable form.)

Footnotes

24 This is a ratio between the semimajor axis and the semiminor axis of the star image. Large elongation usually means the telescope is not stable during exposure; it is either moving or shaking.

25 This is the radius that encloses 90% of the light from this star.

26 EW: W Ursae Majoris–type eclipsing variables; KE: contact systems of early (O–A) spectral type. Their variations are both caused by two ellipsoidal components that are almost in contact and not easy to classify.

27 ACV: α^2 Canum Venaticorum variables, which are main-sequence stars with spectral types from B8 to A7 and displaying strong magnetic fields. Their brightness varies with a period from 0.5 to 160 days and an amplitude within 0.1 mag.

28 http://www.njutido.com/tido/data.html or http://116.62.78.33/tido/data.html

29 http://casdc.china-vo.org/archive/ast3/II/dr1/

References

Ashley M. C. B. 2013 IAU Symp. 288, Astrophysics from Antarctica (Cambridge: Cambridge Univ. Press) 15

Ashley M. C. B., Allen G., Bonner C. S. et al 2010 EAS 40 79

Bakos G., Noyes R. W., Kovács G. et al 2004 PASP 116 266

Baraffe I., Chabrier G. and Barman T. 2008 A&A 482 315

Bertin E. and Arnouts S. 1996 A&AS 117 393

Bertin E., Mellier Y., Radovich M. et al 2002 ASP Conf. Ser. 281, adass XI ed D. A. Bohlender, D. Durand and T. H. Handley (San Francisco, CA: ASP) 228

Bonner C. S., Ashley M. C. B., Cui X. et al 2010 PASP 122 1122

Borucki W. J., Koch D., Basri G. et al 2010 Sci 327 977

Breger M. 2000 ASP Conf. Ser. 210, Delta Scuti and Related Stars (San Francisco, CA: ASP) 3

Burton M. G., Busso M., Fossat E. G. et al 2007 IAUTB 26 188

Burton M. G., Zheng J., Mould J. et al 2016 PASA 33 e047

Catelan M. and Smith H. A. 2015 Pulsating Stars (New York: Wiley-VCH)

Charbonneau D., Allen L. E., Megeath S. T. et al 2005 ApJ 626 523

Collins K. A., Collins K. I., Pepper J. et al 2018 AJ 156 234

Bakos G. Á, Csubry Z., Penev K. et al 2013 PASP 125 154

Cui X., Yuan X. and Gong X. 2008 Proc. SPIE 7012 70122D

Cuypers J., Aerts C., De Cat P. et al 2009 A&A 499 967

Deming D., Seager S., Richardson L. J. and Harrington J. 2005 Natur 434 740

Devor J. 2005 ApJ 628 411

Hartman J. D. and Bakos G. Á 2016 A&C 17 1

Henden A. A., Levine S., Terrell D. and Welch D. L. 2015 AAS Meeting 225 336.16

Henden A. A., Templeton M., Terrell D. et al 2016 yCat 2336

Hu Y., Shang Z., Ashley M. C. B. et al 2014 PASP 126 868

Hu Y., Shang Z., Ma B. and Hu K. 2016 Proc. SPIE 9913 99130M

Kenyon S. L. and Storey J. W. V. 2006 PASP 118 489

Knutson H. A. 2007 Natur 448 143

Kolbas V., Pavlovski K., Southworth J. et al 2015 MNRAS 451 4150

Kovács G., Bakos G. and Noyes R. W. 2005 MNRAS 356 557

Kovács G., Zucker S. and Mazeh T. 2002 A&A 391 369

Lang D., Hogg D. W., Mierle K., Blanton M. and Roweis S. 2010 AJ 139 1782

Lawrence J. S., Ashley M. C. B., Hengst S. et al 2009 RScI 80 064501

Lawrence J. S., Ashley M. C. B., Tokovinin A. and Travouillon T. 2004 Natur 431 278

Liang E.-S., Wang S., Zhou J.-L. et al 2016 AJ 152 168

Liu Q., Wei P., Shang Z.-H., Ma B. and Hu Y. 2018 RAA 18 005

Ma B., Shang Z., Hu Y. et al 2014 Proc. SPIE 9154 91541T

Ma B., Shang Z., Hu Y. et al 2018 MNRAS 479 111

Ma B., Shang Z., Wang L. et al 2012 Proc. SPIE 8446 84466R

Meng Z., Zhou X., Zhang H. et al 2013 PASP 125 1015

Obermeier C., Koppenhoefer J., Saglia R. P. et al 2016 A&A 587 A49

Oelkers R. J., Macri L. M., Wang L. et al 2016 AJ 151 166

Pepper J., Pogge R. W., DePoy D. L. et al 2007 PASP 119 923

Pollacco D. L., Skillen I., Collier Cameron A. et al 2006 PASP 118 1407

Press W. H., Teukolsky S. A., Vetterling W. T. and Flannery B. P. 1992 The Art of Scientific Computing 2nd ed. (Cambridge: Cambridge Univ. Press)

Ricker G. R., Latham D. W., Vanderspek R. K. et al 2009 AAS Meeting 214 306.05

Saunders W., Lawrence J. S., Storey J. W. V. et al 2009 PASP 121 976

Schmidt E. G., Johnston D., Langan S. and Lee K. M. 2004 AJ 128 1748

Schwarzenberg-Czerny A. 1989 MNRAS 241 153

Seager S., Kuchner M., Hier-Majumder C. A. and Militzer B. 2007 ApJ 669 1279

Seager S. and Mallén-Ornelas G. 2003 ApJ 585 1038

Shang Z., Hu K., Hu Y. et al 2012 Proc. SPIE 8448 844826

Shang Z., Hu Y., Ma B. et al 2016 Proc. SPIE 9910 991023

Sharma S., Stello D., Buder S. et al 2018 MNRAS 473 2004

Shi S.-C., Paine S., Yao Q.-J. et al 2016 NatAs 1 0001

Smith H. A. (ed) 2004 RR Lyrae Stars (Cambridge: Cambridge Univ. Press)

Soszynski I., Udalski A., Szymanski M. K. et al 2008 CoAst 157 41

Stassun K. G., Oelkers R. J., Pepper J. et al 2018 AJ 156 102

Stetson P. B. 1996 PASP 108 851

Storey J. W. V., Ashley M. C. B., Burton M. G. and Lawrence J. S. 2005 14 7

Tamuz O., Mazeh T. and Zucker S. 2005 MNRAS 356 1466
Wang L., Ma B., Li G. et al 2017 AJ 153 104
Wang L., Macri L. M., Krisciunas K. et al 2011 AJ 142 155
Wang S., Zhang H., Zhou J.-L. et al 2014a ApJS 211 26
Wang S., Zhang H., Zhou X. et al 2015 ApJS 218 20
Wang S., Zhou X., Zhang H. et al 2012 PASP 124 1167
Wang S.-H., Zhou X., Zhang H. et al 2014b RAA 14 345
Wei P., Shang Z., Ma B. et al 2014 Proc. SPIE 9149 91492H
Welch D. L. and Stetson P. B. 1993 AJ 105 1813
Wheatley P. J., West R. G., Goad M. R. et al 2018 MNRAS 475 4476
Yang M., Zhang H., Wang S. et al 2015 ApJS 217 28
Yang Y., Moore A. M., Krisciunas K. et al 2017 AJ 154 6
Yuan X., Cui X., Gu B. et al 2014 Proc. SPIE 9145 91450F
Yuan X., Cui X., Liu G. et al 2008 Proc. SPIE 7012 70124G
Yuan X., Cui X., Wang L. et al 2015 IAUGA 22 2256923
Yuan X. and Su D.-q. 2012 MNRAS 424 23
Zackay B. and Ofek E. O. 2017 ApJ 836 187
Zechmeister M. and Kürster M. 2009 A&A 496 577
Zhang H., Yu Z., Yang M. et al 2018 ApJS 240 17
Zhou X., Fan Z., Jiang Z. et al 2010 PASP 122 347
Zong W., Fu J.-N., Niu J.-S. et al 2015 AJ 149 84
Zou H., Zhou X., Jiang Z. et al 2010 AJ 140 602